Locally induced Gaussian processes for large-scale simulation experiments

D. Austin Cole[*†]   Ryan Christianson[†]   Robert B. Gramacy[†]

February 5, 2021

Abstract

Gaussian processes (GPs) serve as flexible surrogates for complex surfaces, but buckle under the cubic cost of matrix decompositions with big training data sizes. Geospatial and machine learning communities suggest pseudo-inputs, or inducing points, as one strategy to obtain an approximation easing that computational burden. However, we show how placement of inducing points and their multitude can be thwarted by pathologies, especially in large-scale dynamic response surface modeling tasks. As remedy, we suggest porting the inducing point idea, which is usually applied globally, over to a more local context where selection is both easier and faster. In this way, our proposed methodology hybridizes global inducing point and data subset-based local GP approximation. A cascade of strategies for planning the selection of local inducing points is provided, and comparisons are drawn to related methodology with emphasis on computer surrogate modeling applications. We show that local inducing points extend their global and data-subset component parts on the accuracy–computational efficiency frontier. Illustrative examples are provided on benchmark data and a large-scale real-simulation satellite drag interpolation problem.

1   Introduction

Advancements and expansion of access to supercomputing, algorithms for finite element analysis, particle transport and agent-based modeling, combine in modern times to produce simulation data of an unprecedented magnitude. Yet as modeling fidelity and configuration spaces continue to grow, coverage of representative cases is still sparse. Gaussian process (GP) regression is a common choice to fill in those gaps, emulating or serving as a surrogate for the data-generating mechanism. GP surrogates excel at downstream tasks from optimization to sensitivity analysis due to their out-of-sample predictive accuracy and uncertainty quantification (UQ) capability, and ability to interpolate the response when simulations are deterministic. For a review of computer experiments and surrogate modeling see Santner et al. (2018) or Gramacy (2020).

However, GP inference and prediction calculations scale poorly for large data sets. GPs involve working with a multivariate normal (MVN) distribution whose dimension matches the training data $(\mathbf{X}_N, \mathbf{Y}_N)$ size, N. Matrix decomposition for covariance determinant and

---

[*]Corresponding author: `austin.cole8@vt.edu`
[†]Department of Statistics, Virginia Tech, Blacksburg, VA

inverses is cubic in N. In practice, this means limiting N to the thousands – small by modern standards.

Work from across disciplines where GPs play a fundamental role (machine learning, geostatistics, computer experiments) targets remedies through various approximations. Some methods induce sparsity in the covariance (Titsias 2009a; Aune et al. 2014; Wilson and Nickisch 2015; Gardner et al. 2018b; Pleiss et al. 2018; Solin and Särkkä 2020) or precision matrix (Datta et al. 2016; Katzfuss and Guinness 2021). Others propose divvying up the design space (Kim et al. 2005; Gramacy and Lee 2008) and constructing multiple GPs by divide-and-conquer. Partitioning offers the potential for parallelized multicore computation, productively engaging untapped resources. It also induces statistical independence which can enhance flexibility when response surfaces have regime changes or exhibit other nonstationary behavior.

One framework, developed separately as *pseudo-inputs* in machine learning (e.g., Snelson and Ghahramani 2006) and *predictive processes* in geostatistics (e.g., Banerjee et al. 2008), offers a low-rank approximation. Together, these two ideas are more recently referred to as *inducing point* methods. Rather than measuring covariances between all pairs of N training data points directly, a smaller reference set $\bar{\mathbf{X}}_M$ of $M \ll N$ inducing points or "knots" is used. Woodbury matrix identities make decompositions cubic in M, a potentially dramatic savings. While space-filling work well, optimizing the multitude M and location of knots is fraught with challenges (e.g., Garton et al. 2020).

One thing that sets surrogate modeling of computer simulations apart from machine learning and geostats applications of GPs – beside time being of the essence – is an all-but-total emphasis on prediction and UQ above other inferential tasks. This opens up new opportunities for computational and statistical economies by taking a *transductive* approach to learning (Vapnik 2013): let the testing data dictate how training is done. Accurate, approximate GP prediction at an input $\mathbf{x}^\star$ can be based on a subset of data nearby $\mathbf{x}^\star$, leading to the so-called local approximate GP (LAGP; Gramacy and Apley 2015). Small data subsets $n \ll N$ mean faster matrix decomposition, and potential for embarrassingly parallel implementation (Gramacy et al. 2014), through an infinite divide-and-conquer/partition scheme.

The best sub-designs for predicting at $\mathbf{x}^\star$ depend on the training data $\mathbf{X}_n(\mathbf{x}^\star) \subset \mathbf{X}_N$ nearby $\mathbf{x}^\star$. Those which are the very closest – a nearest neighbor (NN) subset – may not be ideal for all predictive goals, such as minimizing mean-squared error (MSE; Vecchia 1988; Stein et al. 2004). Best results require sequentially optimizing a criterion for each $\mathbf{x}^\star$ to greedily build $\mathbf{X}_n(\mathbf{x}^\star)$. Although speedy and vastly parallelizable, handling N in the millions in a matter of minutes, it can still represent a substantial computational effort, growing cubically with n and combinatorially in $\binom{N}{n}$ choices. Authors have long opined that novel searches for each $\mathbf{x}^\star \in \mathbf{X}$ could be short-cut by learning some kind of re-locatable *template* of local sub-design characteristics (Gramacy and Haaland 2016; Sung et al. 2018). However, a truly thrifty scheme has so far remained elusive.

We believe a potential answer may lie in hybridizing inducing point and local GP schemes – a variation on a recently popular theme of combining sparse GP methods with local models (Tan et al. 2016; Liu et al. 2019). The basic idea is as follows: search locally for m inducing points $\bar{\mathbf{X}}_m(\mathbf{x}^\star)$ in order to predict nearby $\mathbf{x}^\star$, specifically on a NN set $\mathbf{X}_n(\mathbf{x}^\star)$. Having $m \ll n \ll N$ leads to a manageable cascade of calculations. We show how greedy optimization of $\bar{\mathbf{X}}_m(\mathbf{x}^\star)$, via a closed form weighted integrated MSE (wIMSE)

criterion and gradients, avoids combinatorial sub-design search. Moreover, $\bar{\mathbf{X}}_m(\mathbf{x}^\star)$ can be used as a template, relocated anywhere for any $\mathbf{x}^\star$ without re-optimization. In fact, we show that even locally space-filling schemes make for adequate templates in this setting. The result is a *local inducing point GP (LIGP)* approximation which is nearly as accurate as LAGP, sometimes even more accurate, and is faster. Whereas LAGP was limited by small-n neighborhoods regardless of what the data prefer, we show that LIGP is not. We explore neighborhoods more than double the size of LAGP and demonstrate accuracy improvements for commensurate computational effort. This allows the user, for the first time, to fully explore the statistical–computational efficiency Pareto frontier in the context of local GP approximation.

The remainder of the paper is organized as follows. Section 2 provides an overview of GP regression and various scalable models, including local and inducing points methods by way of motivating our hybrid approach. Section 3 describes the joining of local and inducing points methods comprising LIGP. We detail some refinements to LIGP, including local inducing point templates, in Section 4. Illustrative examples are provided throughout, however Section 5 offers a systematic comparison of LIGP and LAGP variations to using both synthetic and real benchmark examples. Section 6 concludes with a discussion.

2 Foundations in GP approximation

Here we highlight relevant surrogate modeling and scalable GP methods and provide motivation for a new criterion for placement of global and local inducing points.

2.1 Gaussian process regression

Consider an unknown function $f : \mathbf{X}_N \subset \mathbb{R}^d \to \mathbb{R}$ for a set of d-dimensional design locations $\mathbf{X}_N = (\mathbf{x}_1, ..., \mathbf{x}_N)^\top$ and corresponding observations $\mathbf{Y}_N = (y_1, ..., y_N)^\top$. GPs are common surrogates for such data (Sacks et al. 1989), especially as arising from deterministic computer simulations $f(\cdot)$, and boil down to placing an MVN prior on the observations $\mathbf{Y}_N$. Gaussians are uniquely defined by a mean vector, which we take as zero for simplicity, and an $N \times N$ covariance matrix $\mathbf{K}_N$. The joint model for all responses is $\mathbf{Y}_N \sim \mathcal{N}_N(\mathbf{0}, \nu(\mathbf{K}_N + \epsilon_k \mathbb{I}_N))$ where ν is a scale hyperparameter and $\mathbf{K}_N$ is comprised of entries based on a kernel $k_\theta(\mathbf{x}_i, \mathbf{x}_j)$. Jitter parameter ϵ_K is set as small as possible (for interpolating deterministic simulations) while maintaining well-conditioned positive-definite covariances (Neal 1998), and $\mathbb{I}_N$ denotes an $N \times N$ identity matrix. Our presentation is agnostic to the choice of $k_\theta(\cdot, \cdot)$ except that it be based on inverse distances in the input space. Our empirical work favors a squared exponential kernel with lengthscale hyperparameter θ.

$$\mathbf{K}_N^{ij} = k_\theta(\mathbf{x}_i, \mathbf{x}_j) = \exp\left\{ -\frac{||\mathbf{x}_i - \mathbf{x}_j||^2}{\theta} \right\} \tag{1}$$

Other common kernels include the Matérn family (Stein 2012; Gramacy 2020, Section 5.3.3).

Inference for unknown hyperparameters (θ, ν) can proceed by maximum likelihood estimation through the log MVN pdf and its closed-form derivatives. Some hyperparameters, like $\hat{\nu} = N^{-1} \mathbf{Y}_N^\top \mathbf{K}_N^{-1} \mathbf{Y}_N$, have tidy expressions conditional on others, like θ, which must be optimized numerically. Since MVN pdfs involve $|\mathbf{K}_N|$ and $\mathbf{K}_N^{-1}$, computation is on the order of $\mathcal{O}(N^3)$, limiting training data sizes N to the small thousands on most desktop machines.

In custom setups with highly distributed architectures, stochastic approximations based on linear conjugate gradients and Lanczos quadrature can push those boundaries (Ubaru et al. 2017; Gardner et al. 2018a; Wang et al. 2019).

For fixed hyperparameters $(\hat{\nu}, \hat{\theta})$ a predictive distribution for $Y(\mathbf{x}^\star)$ arises as standard MVN conditioning via an $(N+1)$-dimensional MVN for $(Y(\mathbf{x}^\star), \mathbf{Y}_N)$. The moments of that Gaussian distribution are:

$$\mu_N(\mathbf{x}^\star) = \mathbb{E}(Y(\mathbf{x}^*) \mid \mathbf{Y}_N) = \mathbf{k}_N^\top(\mathbf{x}^\star)\mathbf{K}_N^{-1}\mathbf{Y}_N$$

$$\sigma_N^2(\mathbf{x}^\star) = \mathbb{V}\mathrm{ar}(Y(\mathbf{x}^\star) \mid \mathbf{Y}_N) = \hat{\nu}\left(k_\theta(\mathbf{x}^\star, \mathbf{x}^\star) - \mathbf{k}_N^\top(\mathbf{x}^\star)\mathbf{K}_N^{-1}\mathbf{k}_N(\mathbf{x}^\star)\right), \tag{2}$$

where $\mathbf{k}_N(\mathbf{x}^\star) = (k_\theta(\mathbf{x}^\star, \mathbf{x}_1), ..., k_\theta(\mathbf{x}^\star, \mathbf{x}_N))^\top$. These calculations are also in $\mathcal{O}(N^3)$, although again linear algebra tricks can mitigate that to an extent.

2.2 Inducing points

A more direct approach to speedy GP approximation in the face of big N is to impose a low-rank structure on covariance. The idea originated with local data subsets for splines (Wahba 1990; Poggio and Girosi 1990), and later was applied to GPs (Smola and Bartlett 2001; Csató and Opper 2002; Seeger et al. 2003). Snelson and Ghahramani (2006) proposed that these reference locations not be restricted to a subset of the data. First attempts at a unifying perspective for sparse approximate GPs were made by Quiñonero and Rasmussen (2005) and Rasmussen and Williams (2006, Chapter 8), with the former referring to these latent reference variables as *inducing inputs*. Outside of the machine learning community, Banerjee et al. (2008) applied similar techniques to develop *predictive processes*. Here we adopt a big-tent inducing points nomenclature.

Let $\bar{\mathbf{X}}_M = (\bar{\mathbf{x}}_1, \ldots, \bar{\mathbf{x}}_M)^\top$ be M inducing points in the same space as $\mathbf{X}_N$, but they need not coincide with any elements of $\mathbf{X}_N$. Notate $\mathbf{K}_M$ as a kernel matrix built from $\bar{\mathbf{X}}_M$ and $k_\theta(\cdot, \cdot)$, e.g., in (1); similarly, write $\mathbf{k}_{NM}$ as cross evaluations of the kernel between $\mathbf{X}_N$ and $\bar{\mathbf{X}}_M$. Most variations on inducing point methods base GP approximations on the so-called Nyström approximation (Williams and Seeger 2001): $\mathbf{K}_N \approx \bar{\mathbf{K}} = \mathbf{k}_{NM}\mathbf{K}_M^{-1}\mathbf{k}_{NM}^\top$. Rather than calculate covariance between all pairs in $\mathbf{X}_N$, instead use $M \ll N$ references $\bar{\mathbf{X}}_M$ to induce a similar structure $\bar{\mathbf{K}}$.

Snelson and Ghahramani (2006) introduced a diagonal correction on the Nyström approximation

$$\mathbf{\Sigma}_N^{(M)} = \nu(\bar{\mathbf{K}} + \epsilon_k\mathbb{I}_N) = \nu\left(\mathbf{k}_{NM}\mathbf{K}_M^{-1}\mathbf{k}_{NM}^\top + \Lambda_N^{(M)} + \epsilon_K\mathbb{I}_N\right) \tag{3}$$

where $\Lambda_N^{(M)} = \mathrm{Diag}\{\mathbf{K}_N - \mathbf{k}_{NM}\mathbf{K}_M^{-1}\mathbf{k}_{NM}^\top\}$. This ensures that $\bar{\mathbf{K}}$ and $\mathbf{K}_N$ contain the same diagonal elements so that when $\bar{\mathbf{X}}_M \equiv \mathbf{X}_N$, $\mathbf{\Sigma}_N^{(M)}$ in (3) reduces to the standard GP covariance $\mathbf{\Sigma}_N = \nu(\mathbf{K}_N + \epsilon_k\mathbb{I}_N)$. Both approximations allow for decomposition of $\mathbf{\Sigma}_N^{(M)}$ through Woodbury matrix identities (Harville 2011):

$$\mathbf{\Sigma}_N^{-1(M)} = \nu^{-1}\left(\Omega_N^{-1(M)} - \mathbf{\Gamma}_{NM}\mathbf{Q}_M^{-1(N)}\mathbf{\Gamma}_{NM}^\top\right) \tag{4}$$

$$\log|\mathbf{\Sigma}_N^{(M)}| = \log(\nu) + \log|\mathbf{Q}_M^{(N)}| - \log|\mathbf{K}_M| + \mathbf{1}_N^\top\log(\Omega_N^{(M)})\mathbf{1}_N,$$

where $\mathbf{\Gamma}_{NM} = \Omega_N^{-1(M)}\mathbf{k}_{NM}$ and $\mathbf{1}_N$ is a vector of N ones. Above, $\mathbf{Q}_M^{(N)} = \mathbf{K}_M + \mathbf{k}_{NM}^\top\Omega_N^{-1(M)}\mathbf{k}_{NM} + \epsilon_Q\mathbb{I}_M$ and $\Omega_N^{(M)} = \Lambda_N^{(M)} + \epsilon_K\mathbb{I}_N$. Since $\Omega_N^{(M)}$ is an $N \times N$ diagonal

matrix and can be stored and manipulated as a vector, we elect to not embolden its notation like that of other matrices. Hyperparameter inference is achieved by maximizing the logarithm of the MVN likelihood $Y_N \sim \mathcal{N}\left(\mathbf{0}, \nu(\mathbf{k}_{NM}\mathbf{K}_M^{-1}\mathbf{k}_{NM}^\top + \Omega_N^{(M)})\right)$:

$$\ell(\mathbf{X}, \mathbf{Y}, \bar{\mathbf{X}}_M, \nu, \theta, g) = -\frac{N}{2}\log(2\pi) - \frac{1}{2}\log|\mathbf{\Sigma}_N| - \frac{1}{2}\mathbf{Y}_N^\top \mathbf{\Sigma}_N^{-1}\mathbf{Y}_N \tag{5}$$

$$\propto \text{const.} - N\log(\nu) - \log|\mathbf{Q}_M^{(N)}| + \log|\mathbf{K}_M| - \mathbf{1}_N^\top \log(\Omega_N^{(M)})\mathbf{1}_N$$

$$- \nu^{-1}\mathbf{Y}_N^\top\left(\Omega_N^{-1(M)} - \mathbf{\Gamma}_{NM}\mathbf{Q}_M^{-1(N)}\mathbf{\Gamma}_{NM}^\top\right)\mathbf{Y}_N.$$

Differentiating Eq. (5) with respect to ν and solving yields the closed-form estimate

$$\hat{\nu}^{(N,M)} = N^{-1}\mathbf{Y}_N^\top\left(\Omega_N^{-1(M)} - \mathbf{\Gamma}_{NM}\mathbf{Q}_M^{-1(N)}\mathbf{\Gamma}_{NM}^\top\right)\mathbf{Y}_N. \tag{6}$$

There is not a similar closed-form solution for the lengthscale. Numerical solvers like `optim` in R can work with negative concentrated log-likelihood

$$-\ell\left(\mathbf{X}, \mathbf{Y}, \bar{\mathbf{X}}_M, \theta\right) \propto N\log\left(\mathbf{Y}_N^\top\left(\Omega_N^{-1(M)} - \mathbf{\Gamma}_{NM}\mathbf{Q}_M^{-1(N)}\mathbf{\Gamma}_{NM}^\top\right)\mathbf{Y}_N\right) \tag{7}$$

$$+ \log|\mathbf{Q}_M^{(N)}| - \log|\mathbf{K}_M| + \mathbf{1}_N^\top\log(\Omega_N^{(M)})\mathbf{1}_N$$

and closed form derivatives (not shown) to obtain $\hat{\theta}^{(N,M)}$. In practice this works well because the surfaces are either convex in hyperparameters, or are nearly so.

Analogues to Eqs. (6–7) reduce full rank prediction from $\mathcal{O}(N^3)$ down to $\mathcal{O}(NM^2)$ flops. Following (3), predictive equations are Gaussian with

$$\mu_{M,N}(\mathbf{x}^\star) = \mathbf{k}_M^\top(\mathbf{x}^\star)\mathbf{Q}_M^{-1(N)}\mathbf{\Gamma}_{NM}^\top\mathbf{Y}_N \tag{8}$$

$$\sigma_{M,N}^2(\mathbf{x}^\star) = \nu\left(\mathbf{K}_{\star\star} - \mathbf{k}_M^\top(\mathbf{x}^\star)\left(\mathbf{K}_M^{-1} - \mathbf{Q}_M^{-1(N)}\right)\mathbf{k}_M(\mathbf{x}^\star)\right),$$

where $\mathbf{k}_M(\mathbf{x}^\star) = k_\theta(\bar{\mathbf{X}}_M, \mathbf{x}^\star)$. When optimizing $\bar{\mathbf{X}}_M$ via log likelihood, the value $\mathbf{Q}_M^{-1(N)}\mathbf{\Gamma}_{NM}^\top\mathbf{Y}_N$ can be re-used from $\mathbf{\Sigma}_N^{-1(M)}\mathbf{Y}_N$. Thus, prediction requires only $\mathcal{O}(M)$ and $\mathcal{O}(M^2)$ additional flops compared to $\mathcal{O}(N)$ and $\mathcal{O}(N^2)$ for a full GP model.

2.3   Optimal induction

Suppose, for now, that the number of inducing points M is fixed by computational limitations. Snelson and Ghahramani (2006) suggested selecting locations $\bar{\mathbf{X}}_M$ through the marginal log-likelihood. Such a strategy is prone to overfitting (Bauer et al. 2016), while the Variational Free Energy (VFE) approximation—a lower bound on the marginal likelihood—is not (Titsias 2009a,b; Hoffman et al. 2013). Yet even with VFE's variational construction of the likelihood, its optimization still requires a cubic cost on a highly-multimodal surface (Bauer et al. 2016), which we explore in Appendix A. This begs the question if likelihood optimization is worth it over relatively convenient space-filling options.

Methods for "choosing inputs", known more widely as statistical design or *active learning*, have potential to reduce the cost of selecting inducing points. A slew of acquisition functions for greedy design point selection are available for such diverse goals as integral estimation (Fernández et al. 2020; Kanagawa and Hennig 2019), space-fillingness (Busby

2009; Svendsen et al. 2020), and posterior density approximation (Wang and Li 2018). Other variance-based (2) criteria may be appropriated for the selection of inducing points $\bar{\mathbf{X}}_M$ by routing through Eq. (8) instead. Such criteria require quadratic computational cost and more squarely target predictive goals in surrogate modeling. In particular, we consider integrated mean-squared error (IMSE) and its discretized analog Active Learning Cohn (Cohn 1993, ALC) to select inducing points $\bar{\mathbf{X}}_M$, a design strategy not yet explored in the literature. See Appendix A for an overview of these variance-based criteria.
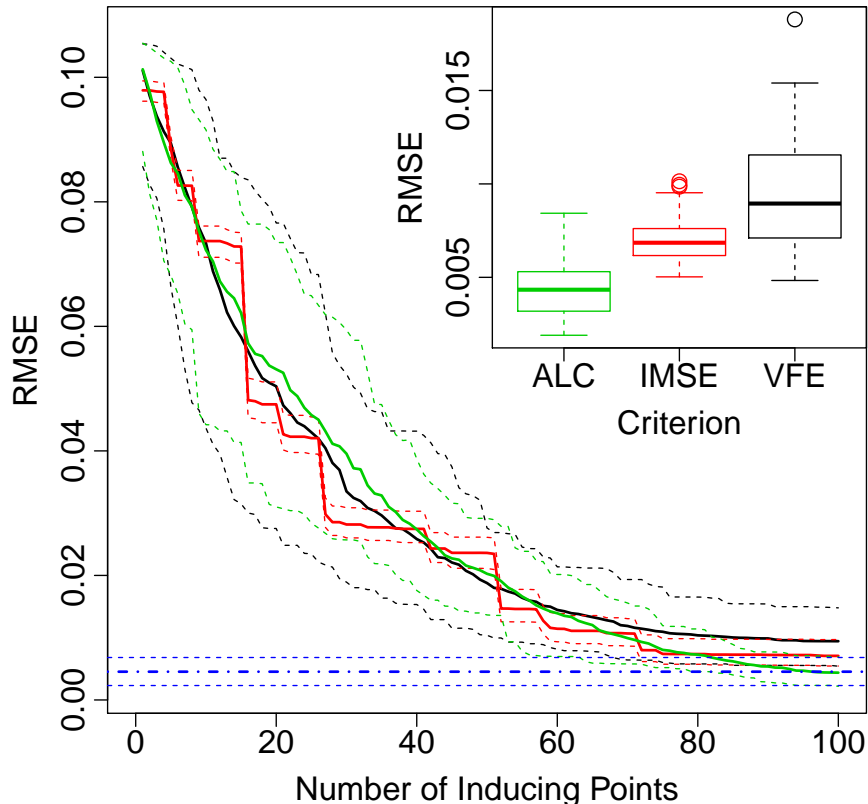

Figure 1: Approximate GP performance via RMSE and number of inducing points, M, compared to a full GP (blue). Means (solid) and central 90% intervals (dashed) arise from thirty replicates. Boxplots in the top right zoom in at $M = 100$.

For a simple experiment, we sought to compare the predictive accuracy of sparse GP models with inducing points selected sequentially with VFE, IMSE, and ALC to a full GP. We generate data using $f(x_1, x_2) = x_1 \exp\{-x_1^2 - x_2^2\}$ for $x_1, x_2 \in [-2, 4]$. Figure 1 compares the three methods to themselves and to a full GP over $M = 1, \ldots, 100$ tracking root MSE (RMSE) via Monte Carlo (MC) averaging over training $\mathbf{X}_N$ and testing $\mathcal{X}$ locations. To manage the computational cost of evaluating criteria on a dense grid, training data sizes were limited to $N = 100$.[1] Observe that all three methods offer a decent approximation to the full GP with close to 85 inducing points. Zoomed boxplots (upper-right panel) show that ALC is consistently best. If you know where you are going to be tested, you should

---

[1]Ordinary IMSE was used, substituting inducing points in for design points, as described in Binois et al. (2019). Progress is blocky because individual inducing point additions do not substantial alter space-filling properties until most of a "new row" of sites are added in this 2d example.

"design" your $\bar{\mathbf{X}}_M$ to focus there. If you do not, then you are (eventually) next-best by integrating over the input domain with IMSE. VFE performs worst because likelihood is imperfectly aligned to the RMSE criteria.

2.4   Local approximate GPs

Rather than massage the GP framework to cope with the entire data set at once, e.g., by working with a single global data subset, a *local approximate GP* (LAGP; Gramacy and Apley 2015) considers disparate local data subsets depending on each of the predictive location(s) $\mathbf{x}^\star$ of interest. Such subsets can be much smaller because, under typical inverse-distance based correlation (1), training data inputs $\mathbf{X}_N$ far from each $\mathbf{x}^\star$ provide little added value to the underlying predictor. Specifically, suppose that $(\mathbf{X}_n(\mathbf{x}^\star), \mathbf{Y}_n(\mathbf{x}^\star))$ represents an n-sized subset, or *neighborhood* of the training data nearby $\mathbf{x}^\star$, e.g., comprised of nearest neighbors (NNs). Then, given a suitable hyperparameterization, prediction could follow Eq. (2) using $(\mathbf{X}_n(\mathbf{x}^\star), \mathbf{Y}_n(\mathbf{x}^\star))$ rather than the full $(\mathbf{X}_N, \mathbf{Y}_N)$. This can potentially provide drastic computational savings when $n \ll N$, even though the calculations would still be cubic in n.

In this framework, the subset size n and neighborhood $\mathbf{X}_n(\mathbf{x}^\star)$ must be determined. Because flops grow quickly with n, this value is usually fixed by computational limitations, just like the number of inducing points, M. A default in the `laGP` software (Gramacy 2016) is $n = 50$, see Appendix B for further discussion. Fixing n, it turns out that NN subdesign, originally suggested by Emery (2009) in a 2d geostatistics setting, is sub-optimal by several criteria (Vecchia 1988; Stein 2012). However, exhaustively searching among all $\binom{N}{n}$ alternatives for each $\mathbf{x}^\star$ is combinatorially infeasible. Gramacy and Apley showed that greedy neighborhood selection via ALC approximately minimizes a MSE criteria common in surrogate modeling settings. Specifically, choose a singleton reference set $\mathcal{X} = \{\mathbf{x}^\star\}$, with $\sigma^2_{\text{new}}(\cdot) = \sigma^2_{n+1}(x)$ derived from $(\mathbf{X}_n(\mathbf{x}^\star), \mathbf{Y}_n(\mathbf{x}^\star))$ and select among $\mathbf{x}_{n+1} \in \mathbf{X}_N \setminus \mathbf{X}_n(\mathbf{x}^\star)$ candidates.[2]

Care is taken to ensure computational demands in each update and ALC optimization do not exceed $\mathcal{O}(n^2)$ so that the entire scheme's flops are not worse in order than using NNs (i.e., cubic in n). For example, if $v_n(\mathbf{x}_{n+1}) = \mathbf{k}_{n+1}(\mathbf{x}_{n+1}, \mathbf{x}_{n+1}) - \mathbf{k}_{n+1}^\top(\mathbf{x}_{n+1})\mathbf{K}_{n+1}^{-1}\mathbf{k}_{n+1}(\mathbf{x}_{n+1})$ represents the kernel portion of $\sigma^2_n(\mathbf{x}_{n+1})$, then the change

$$\begin{aligned}
\Delta v_n(\mathbf{x}^\star) &= v_n(\mathbf{x}^\star) - v_{n+1}(\mathbf{x}^\star) \\
&= \mathbf{k}_n^\top(\mathbf{x}^\star)\mathbf{G}_n(\mathbf{x}_{n+1})v_n(\mathbf{x}_{n+1})\mathbf{k}_n(\mathbf{x}^\star) + 2\mathbf{k}_n^\top(\mathbf{x}^\star)\mathbf{g}_n(\mathbf{x}_{n+1})k_\theta(\mathbf{x}_{n+1}, \mathbf{x}^\star) \\
&\quad + k_\theta(\mathbf{x}_{n+1}, \mathbf{x}^\star)^2/v_n(\mathbf{x}_{n+1})
\end{aligned} \tag{9}$$

can be updated in $\mathcal{O}(n^2)$ via partition inverse equations (Barnett 1979) using $\mathbf{G}_j(\mathbf{x}_{n+1}) = \mathbf{g}_n(\mathbf{x}_{n+1})\mathbf{g}_n^\top(\mathbf{x}_{n+1})$, $\mathbf{g}_n(\mathbf{x}_{n+1}) = -\mathbf{K}_n^{-1}\mathbf{k}_n(\mathbf{x}_{n+1})/v_n(\mathbf{x}_{n+1})$.

Despite being massively parallelizable (Gramacy et al. 2014) for many $\mathbf{x}^\star$ and over candidates $\mathbf{x}_{n+1} \in \mathbf{X}_N \setminus \mathbf{X}_n(\mathbf{x}^\star)$, further approximations are made in order to shortcut $\mathcal{O}(N)$ subroutines in an $\mathcal{O}(n^2)$ scanning over that set (Gramacy and Haaland 2016; Sung et al. 2018; Sun et al. 2019). Several groups of authors have suggested that it might be possible to design a "template" sub-design that could be applied automatically, after simple

---

[2]Here we are abusing notation a little to describe an inductive process $n \to n + 1$ and referring to n as the final local design size as opposed to introducing a new iterator.

shifting/scaling for each $\mathbf{x}^\star$, without exhaustive search of $\mathbf{X}_N \setminus \mathbf{X}_n(\mathbf{x}^\star)$. Non-uniform global designs $\mathbf{X}_N$ render this a non-starter. Sparse design coverage in some regions, and dense in others, demands bespoke calculation in each $\mathbf{x}^\star$ instance. Even with highly regular (e.g., gridded) global designs $\mathbf{X}_N$, local coverage can be irregular at the boundaries.

Local design topology is twinned with subset size, n. Accommodating wiggly test problems benefit with reactive dynamics offered by smaller n is easy, because that means faster execution. But n much larger than the default of $n = 50$ can be a deal-breaker on speed grounds regardless of accuracy boosts in less wiggly settings.

3   Inducing point neighborhoods

Inducing points offer computational savings, but several drawbacks remain. Predictive accuracy suffers when they are placed far from testing locations. Optimization by likelihood can perform worse than simple space-filling (Section 2.3). Computational costs are still cubic in a big number, despite $M \ll N$ because you need enough M to fill the input volume. Multi-processing parallel schemes via likelihood (Chen et al. 2013) and stochastic variational inference (Hensman et al. 2013; Hoang et al. 2015; Schürch et al. 2020) offer limited respite because they operate on the full data.

We thus propose a *locally induced GP (LIGP)* by hybridizing ordinary, "global" inducing point schemes with LAGP. This brings knock-on benefits to the local data-subsetting world: speed-ups, selection of neighborhood size (larger for smoother processes), long-elusive template schemes (Section 4). LIGP operates similarly to LAGP via neighborhoods $\mathbf{X}_n(\mathbf{x}^\star) \subset \mathbf{X}_N$. If a greedy scheme like ALC is used to fill $\mathbf{X}_n(\mathbf{x}^\star)$, it would include an exhaustive search on the order of $\mathcal{O}(Nn^3)$. Instead we choose simple NN approach, incurring an amortized one-off $\mathcal{O}(N \log N)$ cost. Effort is reallocated into choosing local inducing points $\bar{\mathbf{X}}_m(\mathbf{x}^\star)$ for $\mathbf{X}_n(\mathbf{x}^\star)$, which are free to take on any values, at cubic in m cost. Our multiplicity notation is intended to convey $m \ll n \ll M \ll N$, although that hierarchy need not be strict. Small m allows wider local scope with bigger n without a substantial computational hit.

Algorithm 1 outlines the LIGP prediction algorithm, which can be run independently for each $\mathbf{x}^\star \in \mathbf{X}^\star$. For each $\mathbf{x}^\star$, a local neighborhood $\mathbf{X}_n(\mathbf{x}^\star)$ is built from a NN subset of $\mathbf{X}_N$ followed by a set of inducing points $\bar{\mathbf{X}}_m(\mathbf{x}^\star)$. Various methods to select $\bar{\mathbf{X}}_m(\mathbf{x}^\star)$ are explored in the following sections.

Algorithm 1 LIGP Prediction

1: **procedure** LIGP.PRED(m, n, $\mathbf{X}^\star$,$\mathbf{X}_N$,$\mathbf{Y}_N$, $\mathcal{X}$)
2:    **for** $i = 1, \ldots, N' = |\mathbf{X}^\star|$ **do**   ## Each $\mathbf{x}_l^\star \in \mathbf{X}^\star$, potentially in parallel
3:        $\{\bar{\mathbf{X}}_m, \mathbf{X}_n\} \leftarrow$ IP($\ldots$)   ## Any of Algorithms 2–4
4:        $\mathbf{Y}_n \leftarrow Y(\mathbf{X}_n)$ ## Extract from $\mathbf{Y}_N$ at neighborhood
5:        $\hat{\nu}, \hat{\theta} \leftarrow \text{argmax}_{\nu, \theta}$ LLik($\nu, \theta, \mathbf{X}_n, \mathbf{Y}_n, \bar{\mathbf{X}}_m$)   ## Local MLE, Eqs. (6–7)
6:        $\{\hat{\mu}^{(i)}, \hat{\sigma}^{2(i)}\} \leftarrow$ GP.PRED($\mathbf{x}_i^\star \mid \mathbf{X}_n, \mathbf{Y}_n, \bar{\mathbf{X}}_m, \hat{\theta}, \hat{\nu}$)   ## Eq. (8)
7:    **end for**
8:    **return** $\{\hat{\mu}^{(i)}, \hat{\sigma}^{2(i)}\}_{i=1}^{N'}$
9: **end procedure**

3.1 Sequential selection of local inducing points

Changing focus to local neighborhoods $\mathbf{X}_n(\mathbf{x}^\star)$ warrants a second look at selection criteria for inducing points $\bar{\mathbf{X}}_m(\mathbf{x}^\star)$. Likelihoods here are a mismatch to surrogate modeling and machine learning predictive goals. Instead, we follow the LAGP format of greedy optimization via MSE. Given the connection between inducing $\bar{\mathbf{X}}_m(\mathbf{x}^\star)$ and actual training locations $\mathbf{X}_n(\mathbf{x}^\star)$, emphasis on prediction at singleton $\mathbf{x}^\star$ has deleterious effects. We tried this: $\bar{\mathbf{X}}_m(\mathbf{x}^\star)$ "pile up" around $\mathbf{x}^\star$ leading to poor estimates of local lengthscale and curvature. Instead, we suggest a locally weighted IMSE criterion.

Suppose we have $\bar{\mathbf{X}}_m(\mathbf{x}^\star)$ already and wish to choose the next inducing point $\bar{\mathbf{x}}_{m+1}(\mathbf{x}^\star)$. Dependence on $\mathbf{x}^\star$ is implicit below, although we shall drop it from the expressions and simply write $\mathbf{X}_n$, $\bar{\mathbf{X}}_m$ and $\bar{\mathbf{x}}_{m+1}$, etc., in order to streamline the notation. We presume that the study region is a hyperrectangle $\mathcal{X} = [a_k, b_k]_{k=1}^d$. Rather than integrate uniformly over that domain, reproducing an ordinary global IMSE whose closed form slightly generalizes Binois et al. (2019), we weight the calculation by proximity to the predictive location $\mathbf{x}^\star$. Although this weighting scheme could be treated as a tuning parameter, we choose a Gaussian measure proportional to the Gaussian kernel $k_\theta(\cdot, \mathbf{x}^\star)$ to facilitate a similar closed-form solution:

$$\text{wIMSE}_n^{(m+1)}(\bar{\mathbf{x}}_{m+1}, \mathbf{x}^\star) \equiv \text{wIMSE}(\bar{\mathbf{x}}_{m+1}, \mathbf{X}_n, \mathbf{Y}_n, \mathcal{X}, \bar{\mathbf{X}}_m, \mathbf{x}^\star) \tag{10}$$

$$= \int_{\tilde{\mathbf{x}} \in \mathcal{X}} k_\theta(\tilde{\mathbf{x}}, \mathbf{x}^\star) \frac{\sigma_{m+1,n}^2(\tilde{\mathbf{x}})}{\nu} \, d\tilde{\mathbf{x}}$$

$$= \frac{\sqrt{\theta \pi}}{2} \prod_{k=1}^d \left(\text{erf}\left\{ \frac{\mathbf{x}^\star - a_k}{\sqrt{\theta}} \right\} - \text{erf}\left\{ \frac{\mathbf{x}^\star - b_k}{\sqrt{\theta}} \right\} \right) - \text{tr}\left\{ \left(\mathbf{K}_{m+1}^{-1} - \mathbf{Q}_{m+1}^{-1(n)} \right) \mathbf{W}_{m+1}^* \right\},$$

where erf is the error Gaussian function and $\mathbf{W}_{m+1}^\star = \prod_{k=1}^d \mathbf{W}_{m+1,k}^\star$. The $(i,j)^{\text{th}}$ entry of $\mathbf{W}_{m+1,k}^\star$ is

$$w_{m+1,k}^{\star(i,j)} \equiv w_{m+1,k}(\bar{\mathbf{x}}_i, \bar{\mathbf{x}}_j) \tag{11}$$

$$= \int_{a_k}^{b_k} k_\theta(\tilde{\mathbf{x}}_k, \mathbf{x}_k^\star) k_\theta(\tilde{\mathbf{x}}_k, \bar{\mathbf{x}}_{i,k}) k_\theta(\tilde{\mathbf{x}}_k, \bar{\mathbf{x}}_{j,k}) \, d\tilde{\mathbf{x}}_k$$

$$= \sqrt{\frac{\pi \theta}{12}} \exp\left\{ \frac{2}{3\theta} \left(\bar{\mathbf{x}}_{i,k} \mathbf{x}_k^* + \bar{\mathbf{x}}_{j,k} \mathbf{x}_k^* + \bar{\mathbf{x}}_{i,k} \bar{\mathbf{x}}_{j,k} - \mathbf{x}_k^{*2} - \bar{\mathbf{x}}_{i,k}^2 - \bar{\mathbf{x}}_{j,k}^2 \right) \right\}$$

$$\times \left(\text{erf}\left\{ \frac{\iota_k^{(u,j)} - 3a_k}{\sqrt{3\theta}} \right\} - \text{erf}\left\{ \frac{\iota_k^{(u,j)} - 3b_k}{\sqrt{3\theta}} \right\} \right),$$

notating $\mathbf{x}_k^\star$ as the kth entry of the vector $\mathbf{x}^\star$ and $\iota_k^{(u,j)} = \mathbf{x}_k^\star + \bar{\mathbf{x}}_{u,k} + \bar{\mathbf{x}}_{j,k}$. Derivations for (10–11) are included in Appendix A.1. Extensions to other kernel structures, such as Matérn (Stein 2012), yield similar closed forms (i.e., further extending Binois et al. 2019).

The best new local inducing point can be found by solving the following program:

$$\bar{\mathbf{x}}_{m+1} = \text{argmin}_{\bar{\mathbf{x}}_{m+1} \in \mathcal{X}} \text{wIMSE}_n^{(m+1)}(\bar{\mathbf{x}}_{m+1}, \mathbf{x}^\star).$$

The $\text{wIMSE}_n^{(m+1)}(\bar{\mathbf{x}}_{m+1}, \mathbf{x}^\star)$ surface realized over choices $\bar{\mathbf{x}}_{m+1} \in \mathcal{X}$, which we shall visualize momentarily in Section 3.2, may be multi-modal. However, it is not pathologically so like

a global IMSE. Library-based numerical schemes (details in Section 5.1) work well when suitably initialized but perform even better when aided by derivative information. The kth component of the gradient is given by

$$\frac{\partial}{\partial \bar{\mathbf{x}}_{m+1,k}} \text{wIMSE}(\bar{\mathbf{x}}_{m+1}, \mathbf{x}^\star) \tag{12}$$

$$= -\text{tr}\left\{ \left(\frac{\partial \mathbf{K}_{m+1}^{-1}}{\partial \bar{\mathbf{x}}_{m+1,k}} - \frac{\partial \mathbf{Q}_{m+1}^{-1(n)}}{\partial \bar{\mathbf{x}}_{m+1,k}} \right) \mathbf{W}_{m+1}^\star \right\} - \text{tr}\left\{ \left(\mathbf{K}_{m+1}^{-1} - \mathbf{Q}_{m+1}^{-1(n)} \right) \frac{\partial \mathbf{W}_{m+1}^\star}{\partial \bar{\mathbf{x}}_{m+1,k}} \right\}.$$

The form of $\mathbf{W}_{m+1}^\star$, given in Eq. (11), reveals that the only non-zero entries in $\frac{\partial \mathbf{W}_{m+1}^\star}{\partial \bar{\mathbf{x}}_{m+1,k}}$ are the $m+1^{\text{st}}$ row/column. Those entries are

$$\frac{\partial w_{m+1}^\star(\bar{\mathbf{x}}_i, \bar{\mathbf{x}}_{m+1})}{\partial \bar{\mathbf{x}}_{m+1,k}} \prod_{k=1, k \neq k'}^{d} w_{m+1,k}^\star(\bar{\mathbf{x}}_i, \bar{\mathbf{x}}_{m+1}).$$

Derivation of $\frac{\partial w_{m+1}^\star(\bar{\mathbf{x}}_i, \bar{\mathbf{x}}_{m+1})}{\partial \bar{\mathbf{x}}_{m+1,k'}}$ based on a squared exponential kernel is in Appendix A.1.

Expressions for wIMSE and derivative (10–12) leverage the same Woodbury identities used earlier (4–8). Partitioned inverse updates of $\mathbf{K}_{m+1}^{-1}$ and $\mathbf{Q}_{m+1}^{-1(n)}$ (Appendix A.1), allows $m \rightarrow m+1$ in $\mathcal{O}(m^2 n)$ flops.

3.2 Illustrations of Greedy Inducing Point Search

Greedily optimizing wIMSE to place local inducing points around neighborhood $\mathbf{X}_n(\mathbf{x}^\star)$ results in $\bar{\mathbf{X}}_m(\mathbf{x}^\star)$ with (approximately) minimal predictive variance nearby $\mathbf{x}^\star$, so naturally they concentrate in that locale. To explore inducing point optimization with wIMSE, we use a toy 2d test problem known as Herbie's tooth (Lee et al. 2011). This function is attractive due to its low dimensionality but complex nonstationary surface littered with local minima. The function is defined by $f(x_1, x_2) = -w(x_1)w(x_2)$ where $w(x) = \exp\left\{-(x-1)^2\right\} + \exp\left\{-0.8(x+1)^2\right\} - 0.05 \sin\left(8(x+0.1)\right)$ and $x_1, x_2 \in [-2, 2]$. Figure 2 shows the evolution of wIMSE-based acquisition for $\mathbf{x}^\star$ placed at the origin for Herbie's tooth ($N = 40\text{K}$, $n = 100$). Panels (a–c) show existing $\bar{\mathbf{X}}_m(\mathbf{x}^\star)$ in blue overlayed on the wIMSE surface used to select $\bar{\mathbf{x}}_{m+1}$. Optimal $\bar{\mathbf{x}}_{m+1}$, i.e., the wIMSE global minimum, are represented by white-filled circles. Unlike global VFE likelihood, ALC, and IMSE surfaces (explored in Appendix, A, Figure 9), the local wIMSE surface does not appear to be as affected by placement of the training points $\mathbf{X}_N$, or local neighborhood $\mathbf{X}_n(\mathbf{x}^\star) \subset \mathbf{X}_N$, shown as dots in panel (d). Local minima still exist as more inducing points are introduced. Yet the wIMSE surface is much smoother and well-behaved, making optimization easier.

The first selection, $\bar{\mathbf{x}}_1(\mathbf{x}^\star)$, often lies very close to $\mathbf{x}^\star$. When $\mathbf{x}^\star$ is near the boundary of the input space, where wIMSE would be asymmetric, the first inducing point selection may "pull away" somewhat from $\mathbf{x}^\star$ towards to middle of the space. But when symmetry is high, as it is at the origin for the illustration in Figure 2, it is hard to distinguish between $\bar{\mathbf{x}}_1$ and $\mathbf{x}^\star$ up to numerical error. We find it convenient to simply begin optimizing at iteration two, with $\bar{\mathbf{x}}_1 = \mathbf{x}^\star$.

For concreteness, steps for this greedy wIMSE inducing point search are outlined in Algorithm 2. After building the local neighborhood $\mathbf{X}_n(\mathbf{x}^\star)$, initialization is completed by choosing $\bar{\mathbf{x}}_1 \leftarrow \mathbf{x}^\star$ and local lengthscale $\theta^{(0)}$. Here we set $\theta^{(0)}$ based on quantiles of squared

10

(a) wIMSE for 2nd inducing point

(b) wIMSE for 4th inducing point

(c) wIMSE for 10th inducing point

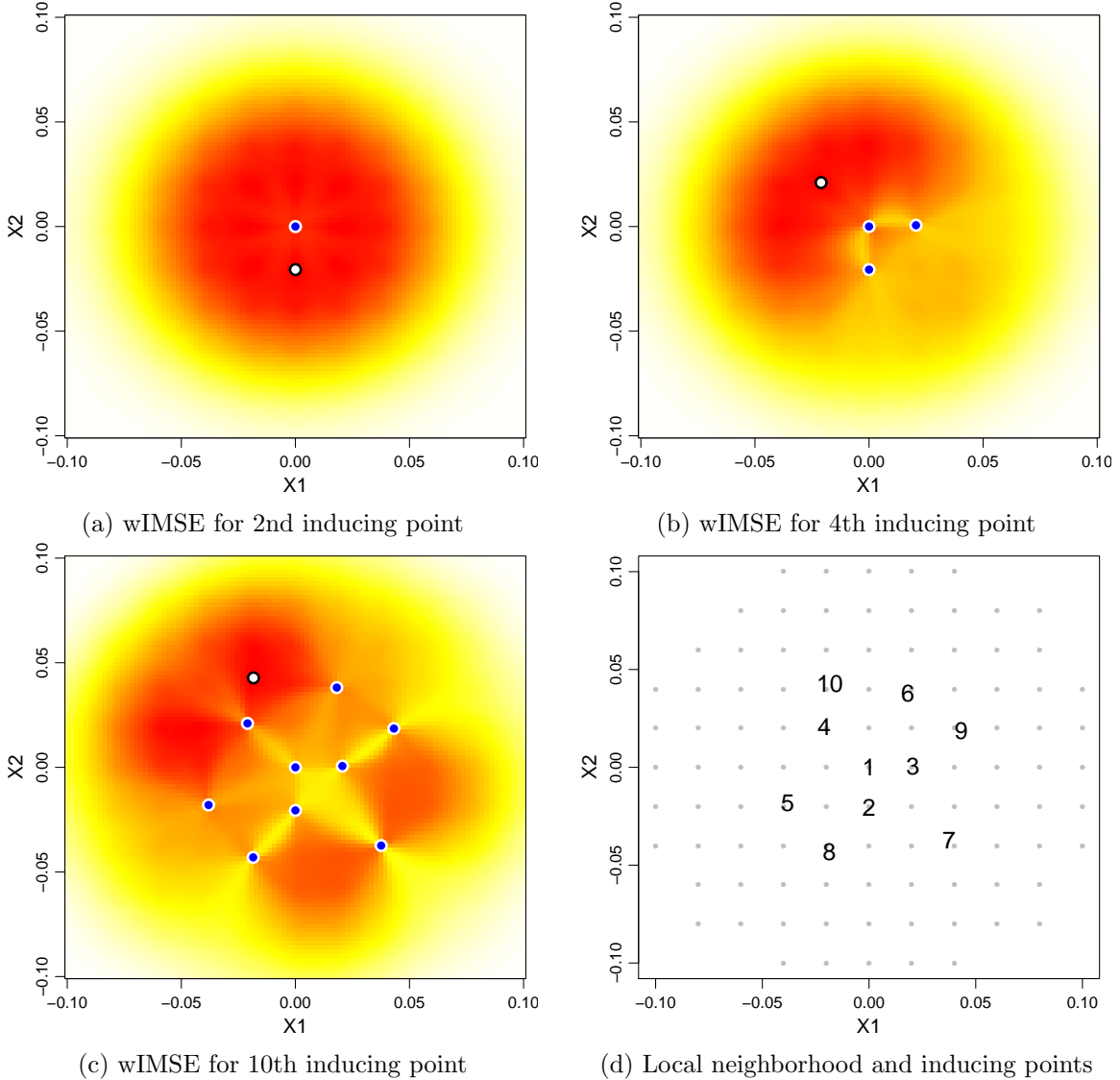(d) Local neighborhood and inducing points

Figure 2: wIMSE surfaces (a–c), red/lower yellow/higher, used to optimize the 2nd, 4th, and 10th inducing points: existing in blue; new selection in white. Predictive location $\mathbf{x}^\star$ is at the origin, which is where $\bar{\mathbf{x}}_1$ is placed. Panel (d) summarizes the neighborhood $\mathbf{X}_n(\mathbf{x}^\star)$ as gray dots and local inducing points $\bar{\mathbf{X}}_m(\mathbf{x}^\star)$ in number order.

distances in $\mathbf{X}_n(\mathbf{x}^\star)$, though other settings are considered later. After greedy selection over $i = 1, \ldots, m$, intermixed with updates to the locally induced GP structure as outlined in Section 3.1, the procedure returns an $m \times d$ matrix comprised of the selected inducing points $\bar{\mathbf{X}}_m(\mathbf{x}^\star)$ alongside an $n \times d$ matrix defining the local neighborhood $\bar{\mathbf{X}}_n(\mathbf{x}^\star)$.

The left panel of Figure 3 shows the predictions for a grid of $\mathbf{x}^\star$ settings arranged over a 1d slice of Herbie's tooth where $x_2^\star = 0.6$, including LAGP (via ALC with $n = 50$, defaults in laGP) and LIGP $(m, n) = (10, 100)$, with local subset and inducing point designs re-optimized at each predictive location. We allow LIGP a bigger neighborhood (n), with explanation in Appendix B, but remind that this involves thriftier m-sized cubic

Algorithm 2 Inducing Point wIMSE Design

1: **procedure** IP.wIMSE(m, n, $\mathbf{x}^\star$, $\mathbf{X}$, $\mathcal{X}$)
2:     $\mathbf{X}_n \leftarrow \text{NN}(\mathbf{x}^\star, \mathbf{X}, n)$ ## Find n nearest neighbors to $\mathbf{x}^\star$
3:     $\theta^{(0)} \leftarrow \text{quantile}(0.1, \text{dist}(\mathbf{X}_n))$ ## Reasonable local lengthscale
4:     $\bar{\mathbf{x}}_1 \leftarrow \mathbf{x}^\star$;   ## Place first inducing point
5:     **for** $i = 2, \ldots, m$ **do**   ## Greedy wIMSE to find the rest
6:         $\bar{\mathbf{x}}_i \leftarrow \text{argmin}_{\bar{\mathbf{x}}_i \in \mathcal{X}} \text{wIMSE}_n^{(i)}(\bar{\mathbf{x}}_i, \mathbf{x}^\star)$ ## Implicit dependence on $\theta^{(0)}$
7:     **end for**   ## Implicit updates of local induced GP
8:     **return** $\bar{\mathbf{X}}_m(\mathbf{x}^\star) = \{\bar{\mathbf{x}}_i\}_{i=1}^m$ and $\mathbf{X}_n(\mathbf{x}^\star) = \mathbf{X}_n$
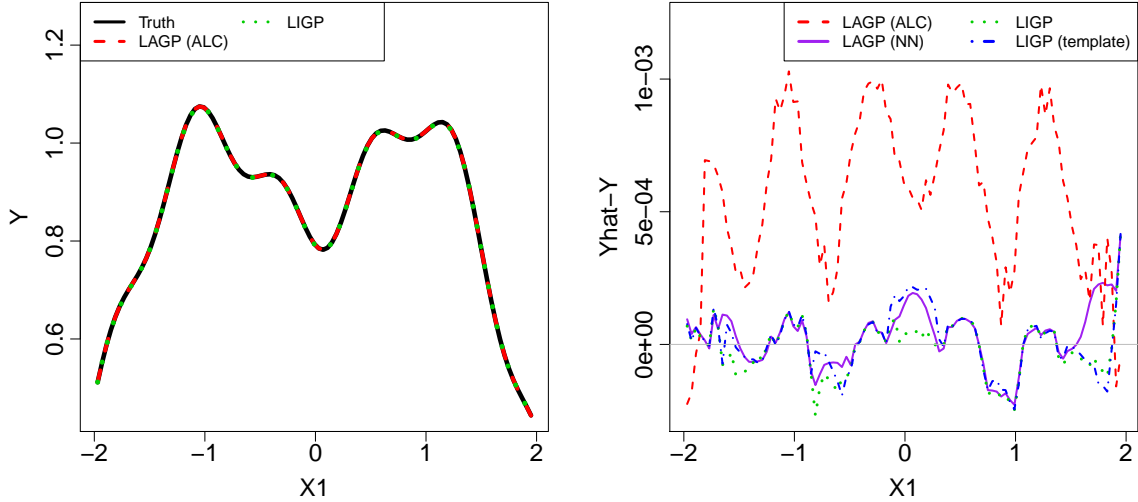9: **end procedure**

Figure 3: *Left*: approximate GP fits' mean prediction and truth on a slice of Herbie's tooth at $x_2^\star = 0.6$. *Right*: errors relative to the truth on the approximate GP fits for the same slice of Herbie's tooth.

decompositions. Observe that both LAGP (red-dashed) and LIGP (green-dotted) capture the bumpiness of the surface, completely overlaying the true out-of-sample response (black-solid).

Zooming in, the right panel of Figure 3 shows errors along the slice under these comparators and two new variations: LAGP via NN with $n = 100$ and LIGP with $(m, n) = (10, 100)$ via template (Section 4.1). Along most of the slice, LIGP's error follows a similar trend as LAGP (NN, $n = 100$), albeit with a bumpier line. This is not surprising given that both GP fits use the same neighborhood $\mathbf{X}_n(\mathbf{x}^\star)$. LAGP (ALC) copes well with smaller $n = 50$ by filling $\mathbf{X}_n(\mathbf{x}^\star)$ with a mix of NNs and satellites.[3] Averaging along that slice, out-of-sample RMSE for LAGP (ALC) was 7.88×10^{-4}, versus 1.14×10^{-4} and 1.12×10^{-4} for LAGP (NN) and LIGP, respectively. Here, LIGP predicts slightly better than LAGP (NN), its most direct competitor, and noticeably better than LAGP (ALC). By reducing the computational burden of the optimization criteria (NN v. ALC) and matrix inversions (LIGP v. LAGP), we free up resources to increase n and thus accuracy.

---

[3]For identical n, ALC bests NN (Gramacy and Apley 2015), motivating increased n for NN here.

Encouraging as these early LIGP results are, selecting novel $\bar{\mathbf{X}}_m(\mathbf{x}^\star)$ for each $\mathbf{x}^\star$ is a substantial undertaking. LIGP required 3.32 seconds, on average, to greedily build $\bar{\mathbf{X}}_m(\mathbf{x}^\star)$ using about 9 derivative-based iterates at each $\mathbf{x}^\star$. Once in hand, optimizing via likelihood using a local analog of Eq. (3) and predicting (8) based on $\bar{\mathbf{X}}_m(\mathbf{x}^\star)$ and $\mathbf{X}_n(\mathbf{x}^\star)$ is almost instantaneous, requiring 0.0062 seconds per prediction. LAGP (NN or ALC), which search discretely over subsets, lag a little behind at 0.0437 and 0.073 seconds, respectively.

4   Refinements to neighborhood composition

LIGP can be accelerated with little impact on predictive accuracy by applying a single inducing point design $\bar{\mathbf{X}}_m(\mathbf{x}^\star)$ almost identically over all predictive locations $\mathbf{x}^\star \in \mathcal{X}$ of interest. Here we explore the benefits of inducing point design templates built with wIMSE and thriftier space-filling strategies.

4.1   Inducing points template

Creating $\bar{\mathbf{X}}_m(\mathbf{x}^\star)$ based on wIMSE for each $\mathbf{x}^\star \in \mathcal{X}$ is a chore that can cannibalize any benefit that might come with adopting an inducing point approximation in the first place. The highly structured nature of optimal wIMSE-based inducing points (Figure 2d) suggests such effort might be overkill. Perhaps the cost of a single, representative optimization could be amortized over the expense of its application on a vast predictive grid. When re-purposed, through shifting or other transformation for new $\mathbf{x}^\star$, we refer to the original wIMSE design – which might be calculated at the middle of the input space – as a *template*.
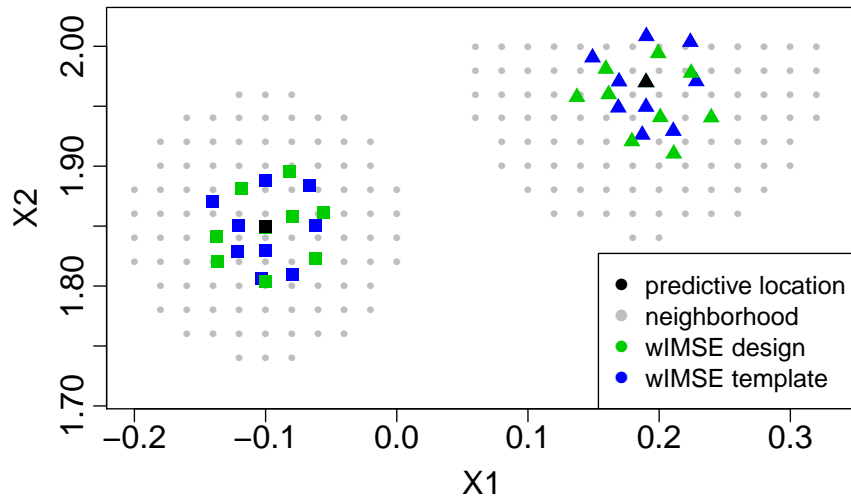

Figure 4: Local neighborhoods for two predictive locations $\mathbf{x}^\star$ at $(-0.1,\ 1.85)$ and $(0.19,$ $1.97)$. Gray dots are $n = 100$ neighborhoods $\mathbf{X}_n(\mathbf{x}^\star)$. Green points are wIMSE optimal inducing points $\bar{\mathbf{X}}_m(\mathbf{x}^\star)$; blue ones are displaced templates derived at the origin. The wIMSE template performs nearly the same space-filling effect as the locally optimized inducing points.

Figure 4 depicts the essence of the idea, comparing bespoke $\bar{\mathbf{X}}_m(\mathbf{x}^\star)$ to re-shifted ones from a template in two variations. The setup is again Herbie's tooth in $[-2, 2]^2$ and the

two predictive sites are $\mathbf{x}^{\star(1)} = (-0.1, 1.85)$ and $\mathbf{x}^{\star(2)} = (0.19, 1.97)$ whose $n = 100$ neighborhoods $\mathbf{X}_n(\mathbf{x}^{\star(1)})$ and $\mathbf{X}_n(\mathbf{x}^{\star(2)})$, shown as gray dots, reside completely in the interior and on the x_2 boundary, respectively. Blue points in the plot represent a wIMSE-based inducing point design – as optimized (Section 3) at the center of the design space and then – shifted to be centered at the $\mathbf{x}^\star$s. Compare these template-based local inducing points to corresponding optimal analogues in green. At both predictive locations, the pair of inducing point designs differ, yet both still space-fill the inner-neighborhood around $\mathbf{x}^\star$. A mild exception may be template-based $\bar{\mathbf{X}}_m(\mathbf{x}^{\star(2)})$ with its two points outside of the design region, which would not happen under an exhaustive re-optimization. Other differences between alternatives would otherwise appear to be cosmetic up to rotation/small perturbations as may stem from a myriad of benign causes: relationship of $\mathbf{x}^\star$ to its local neighborhood $\mathbf{X}_n(\mathbf{x}^\star)$, convergence and global scope in greedy optimization, etc.

Looking back at the right panel of Figure 3, observe how prediction errors based on templates (blue dashed line) compare with locally wIMSE-optimized inducing points (green dotted line) along the slice. Both LIGP variations seem to underestimate the response compared to LAGP (NN), but the template methods give nearly as accurate predictions as LIGP with locally wIMSE-optimized inducing points. Transferring a template captures most of the variability between local wIMSE designs, even at the boundaries. The template is also much faster. It took a total of 328.82 seconds to fit separate $\bar{\mathbf{X}}_m(\mathbf{x}^\star)$ and predict at the 99 $\mathbf{x}^\star$ locations depicted in the slice. Using a template instead takes 3.82 seconds, a near two orders of magnitude improvement.

Algorithm 3 Building and Displacing Inducing Point Templates

1: $\check{\mathbf{x}} \leftarrow \text{median}(\mathbf{X})$ \#\# Set $\check{\mathbf{x}}$ to the center of the data
2: $\bar{\mathbf{X}}_m \leftarrow \text{IP.wIMSE}(m, n, \check{\mathbf{x}}, \mathbf{X}, \mathcal{X})$ \#\# Use Alg. 2 on $\check{\mathbf{x}}$
3: $\bar{\mathbf{X}}'_m \leftarrow \bar{\mathbf{X}}_m - \check{\mathbf{x}}$ \#\# Center template at the origin
4: **procedure** IP.TEMPLATE(n, $\mathbf{x}^\star$, $\mathbf{X}$, $\bar{\mathbf{X}}'_m$)
5:      $\mathbf{X}_n \leftarrow \text{NN}(x^\star, \mathbf{X}, n)$
6:      $\bar{\mathbf{X}}_m \leftarrow \bar{\mathbf{X}}'_m + \mathbf{x}^\star$ \#\# Simple displacement
7:      **return** $\bar{\mathbf{X}}_m(\mathbf{x}^\star) = \{\bar{\mathbf{x}}_i\}_{i=1}^m$ and $\mathbf{X}_n(\mathbf{x}^\star) = \mathbf{X}_n$
8: **end procedure**

Algorithm 3 provides pseudo-code for this template scheme, clarifying how a single wIMSE-based local inducing point design $\bar{\mathbf{X}}_m$ is displaced for each $\mathbf{x}^\star$. It is worth remarking that the scheme makes a tacit presumption that the full design structure, $\mathbf{X}_N$, is somewhat homogeneous: similar near the middle of the input space, $\check{\mathbf{x}}$, as near where it will be applied, i.e., for many disparate $\mathbf{x}^\star \in \mathcal{X}$. We do not doubt it would be possible to engineer test problems, and/or non-space-filling designs $\mathbf{X}_N$, that would thwart this scheme, yet we find it works well in most cases.

4.2 Space-filling templates

Our template-scheme leverages the neighborhood-focused space-filling nature of inducing points, beyond say $\bar{\mathbf{x}}_1 \approx \mathbf{x}^\star$. Space-fillingness is a cornerstone of (global) computer experiment design. Numerous schemes exist, such as Latin hypercube samples (LHSs Mckay et al. 1979) or maximin designs (Johnson et al. 1990), etc., and hybrids thereof (Morris and Mitchell 1995). These work well and often require less computation than model-based

alternatives such as IMSE. If such space-filling designs (SFDs) could be re-tooled to "focus" on particular parts of the input space – say in the neighborhood of $\mathbf{x}^\star$ – we might be able to avoid an expensive greedy wIMSE optimization all together. SFDs might be able to mimic the behavior of a wIMSE template scheme at almost no cost at all.

SFDs are usually constructed in a unit hypercube. Re-centering such a template to $\mathbf{x}^\star$ is trivial, but re-scaling so that it lies within $\mathbf{X}_n(\mathbf{x}^\star)$ and resembles $\bar{\mathbf{X}}_m(\mathbf{x}^\star)$ is more challenging. One way is to derive a second, local rectangle as a means of defining a linear mapping between scales. A thrifty strategy is to use the bounds of the neighborhood $\mathbf{X}_n(\mathbf{x}^\star)$. But the shape of $\mathbf{X}_n(\mathbf{x}^\star)$ is roughly spherical, being comprised of Euclidean distance-based NNs. Thus the rectangular SFD will cover regions outside of the hypersphere, potentially placing some inducing points outside the neighborhood. In low input dimension, say $d \le 2$, this is no big deal, because the circumscription is relatively tight. But when $d = 8$, say, circumscription is poor.

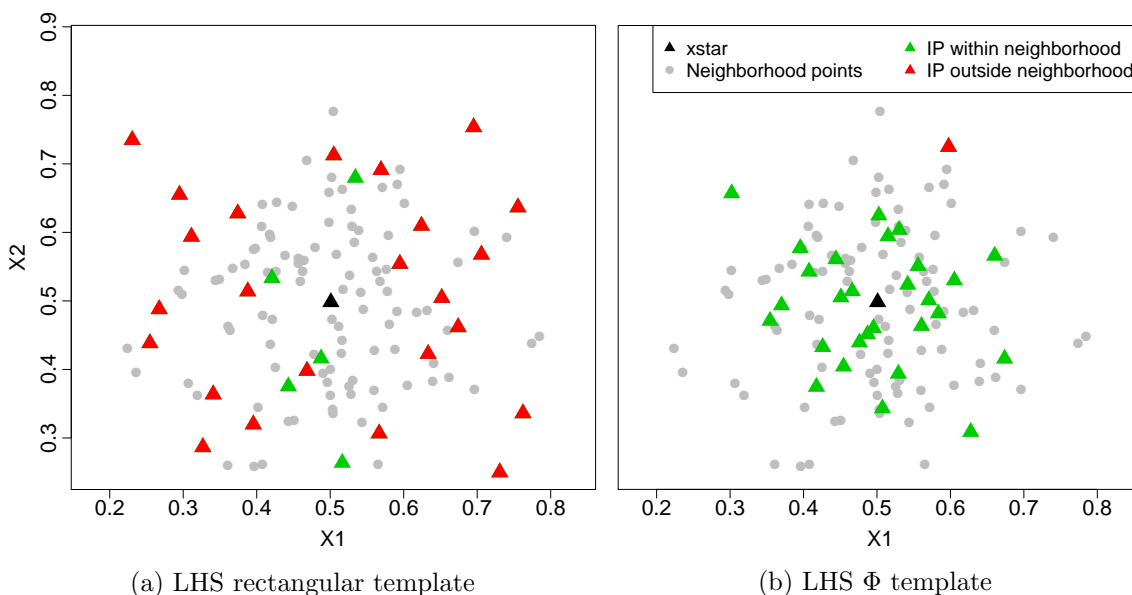(a) LHS rectangular template   (b) LHS Φ template

Figure 5: SFD template schemes (triangles) in 2d projections relative to local neighborhood (gray dots): (a) rectangular re-scaled LHS template (triangles) in relation to a local neighborhood (gray dots); (b) qNorm LHS template. Green triangles indicate $\bar{\mathbf{X}}_m(\mathbf{x}^\star)$ within the neighborhood $\mathbf{X}_n(\mathbf{x}^\star)$ in all coordinates; red outside.

Figure 5a shows a 2d projection of an 8d local neighborhood for the borehole problem, described in Section 5.2. Here, the volume of the convex hull of the neighborhood $\mathbf{X}_n(\mathbf{x}^\star)$ is less than one sixtieth of the size of the rectangle circumscribing its bounds in the coordinate axis directions. Consequently many of the template re-scaled local inducing points $\bar{\mathbf{X}}_m(\mathbf{x}^\star)$, indicated as triangles, lie outside the neighborhood (red) in at least one of the eight coordinates. Of the $m = 30$ local inducing points calculated for that figure, one of which is automatically at $\mathbf{x}^\star$, only five rectangular re-scaled LHS template points lie within the neighborhood.

As remedy, we propose a nonlinear mapping that warps the SFD to lie inside the neighborhood with high probability. In particular, we scale the SFD based on an inverse Gaussian CDF (Φ^{-1}), applied separately to each of the d input coordinates. Algorithm 4

15

outlines steps towards generating an inducing point design $\bar{\mathbf{X}}_m(\mathbf{x}^\star)$ based on a SFD $\hat{\mathbf{X}}$ of size $m - 1$, i.e., beyond choosing $\bar{\mathbf{x}}_1 = \mathbf{x}^\star$. Φ^{-1} calculations for each dimension $k = 1, \ldots, d$ involve $\mu = \mathbf{x}_k^\star$ and variance $\theta^{(0)}$. This is the same $\theta^{(0)}$ as in Algorithm 2 for greedy wIMSE optimization, except here we demonstrate a more absolute default choice. This Φ^{-1} transformation yields higher density near $\mathbf{x}^\star$ and much lower density outside of the neighborhood's hypersphere. Observe in Figure 5b how this warping drastically reduces the number of template points outside of the neighborhood.

Algorithm 4 Inverse Gaussian CDF Space-Filling Template

1: **procedure** IP.qNORM(m, n, $\mathbf{x}^\star$, $\mathbf{X}$)
2:     $\mathbf{X}_n \leftarrow \text{NN}(\mathbf{x}^\star, \mathbf{X}, n)$ ## Find n nearest neighbors to $\mathbf{x}^\star$
3:     $\theta^{(0)} \leftarrow (\frac{1}{3} \max_k |\mathbf{X}_{n,k}(\mathbf{x}^\star) - x_k^\star|)^2$ ## Reasonable local lengthscale
4:     $\hat{\mathbf{X}} \leftarrow \text{SFD}[0, 1]^d$ with $m - 1$ points   ## Could be moved outside
5:     **for** $k = 1, \ldots, d$ **do**   ## Warp each input coordinate
6:         $\breve{\mathbf{x}}_d \leftarrow \Phi^{-1}(\hat{\mathbf{x}}_d; \mu = x_d^\star, \sigma^2 = \theta^{(0)})$ ## Inverse Gaussian CDF with μ, σ^2
7:     **end for**
8:     $\bar{\mathbf{X}}_m \leftarrow \text{rowbind}(\mathbf{x}^\star, \breve{\mathbf{X}})$ ## Add $\mathbf{x}^\star$ as inducing point
9:     **return** $\bar{\mathbf{X}}_m(\mathbf{x}^\star) = \bar{\mathbf{X}}_m$ and $\mathbf{X}_n(\mathbf{x}^\star) = \mathbf{X}_n$
10: **end procedure**

Pseudocode in Algorithm 4 conveys bespoke SFD within each application of the subroutine, yielding new $\hat{\mathbf{X}}$ in each call. As with the wIMSE template in Algorithm 3, this can be moved outside the subroutine to fix a single SFD, which might be important if the SFD is expensive to compute. We prefer LHSs for our SFDs because they are easy/instantaneous via libraries such as `lhs` (Carnell 2019) on CRAN. Hybrids such as maximin–LHS are also straightforward (also with `lhs`), which can avoid some pathologies inherent in random LHS design. Ordinary maximin can be problematic under Φ^{-1} because that criteria places points on the bounding hypercube, which would warp to $\pm\infty$ without intervention, and because evaluating and optimizing that criteria is slow. Uniformly random design may be preferred when local lengthscales are difficult to estimate (Zhang et al. 2021).

Section 3.2 offered comparison between run time and predictive accuracy for LIGP, using wIMSE to build unique inducing point designs, to that of LAGP on a slice of Herbie's tooth. Now consider new template comparators: hyperrectangular SFD, LIGP (cHR), and Φ^{-1}-scaled SFD, LIGP (qNorm). While it took 3.32 seconds on average to build wIMSE-based designs, scaling an SFD to circumscribe the neighborhood (cHR) or applying Φ^{-1} (qNorm) only takes 0.01 seconds on average. Both of these SFD template schemes produce an RMSE that is essentially the same (1.8×10^{-4}) as applying the wIMSE template scheme.

The borehole problem uses larger $(m, n) = (80, 150)$ settings due to the higher input dimension (see Appendix B for a discussion). It takes 141 seconds to build a wIMSE-based inducing point template of size m, while it only takes 0.034 seconds to build a SFD-scaled template. SFD and wIMSE templates produce LIGPs with similar RMSEs, discussed in Section 5.2.

5 Computation and benchmarking

Here we provide implementation details followed by in-depth comparison of LIGP and various template schemes, to LAGP on a swath of synthetic and real computer simulation experiments. Our metrics for benchmarking are out-of-sample RMSE and computation time. All analysis was performed on an eight-core hyperthreaded Intel i9-9900K CPU at 3.60GHz.

5.1 Implementation details

R code (R Core Team 2020) supporting our methodological contribution, and all examples, may be found on our Git repository.

<div align="center">

`https://bitbucket.org/gramacylab/lagp/src/master/R/inducing/`

</div>

Some noteworthy aspects of that implementation include the following. Unlike `laGP`, which is coded in `C` with `OpenMP` for symmetric multiprocessing parallelization (R serving only as wrapper), our LIGP implementation is pure R. Nevertheless, our template schemes are competitive, time-wise, and sometimes notably faster.

We privilege an isotropic Gaussian kernel formulation with scalar lengthscale θ for local modeling, although there is no reason other forms, such as Matérn (Stein 2012), could not be entertained so long as the structure is differentiable with respect to inducing points $\bar{\mathbf{X}}_m$. To improve numerical conditioning of matrices $\mathbf{K}_m$ and $\mathbf{Q}_m^{(n)}$ for stable inversion, we augment their diagonals with $\epsilon_K = 10^{-6}$ and $\epsilon_Q = 10^{-5}$ jitter (Neal 1998), respectively. While both are theoretically decomposible, we find that $\mathbf{Q}_m^{(n)}$ is more sensitive to conditioning issues, thus requiring larger ϵ. In the context of LAGP, it has been shown that separable local formulations do not much improve predictive performance, especially after first applying a global pre-scaling of inputs (Sun et al. 2019). Such stretching and compressing of inputs,[4] has recently become popular as a means of boosting predictive performance of approximate GP methods (e.g., Katzfuss et al. 2020). When pre-scaling in our exercises to ensure apples-with-apples comparisons to benchmarks we divide by square-root separable global lengthscales obtained from a GP's fit to random size-1000 data subsets. See Gramacy (2020), Section 9.3.4, for details. The time required is not included in our summaries.

Building of wIMSE inducing point designs $\bar{\mathbf{X}}_m(\mathbf{x}^\star)$ and templates $\bar{\mathbf{X}}_m(\check{\mathbf{x}})$, generically $\bar{\mathbf{X}}_m$ below, follows Algorithm 3 with m and n appropriate to the input dimension d (Appendix B), provided momentarily with our particular exercises. For initial local lengthscale $\theta^{(0)}$, we have had success with a number of heuristics which often lead to similar values/performance for LIGP methods in our exercises. Gramacy (2016) suggests the 10% quantile of squared pairwise distances between the neighborhood points $\mathbf{X}_n$.[5] See Algorithm 2. A downside is that this is quadratic in n. A more absolute/direct $\mathcal{O}(n)$ approach matches $\theta^{(0)} = \sigma^2$, where 3σ approximates the 99% quantile of a Gaussian fit, to the margins of $\mathbf{X}_n$. Algorithm 4 exemplifies this choice for contrast, although we see these as interchangeable. Each $\bar{\mathbf{x}}_{m+1}$ augmenting $\bar{\mathbf{X}}_m$ optimizing wIMSE is found via a 20-point multi-start L-BFGS-B (Byrd et al. 1995) scheme (using `optim` in R) peppered within the bounding box

---

[4]A characterization attributed to Derek Bingham predating any published account, to our knowledge.

[5]In `laGP`, the function providing $\theta^{(0)}$ in this way is `darg`.

surrounding the neighborhood $\mathbf{X}_n$ to a tolerance of 0.01. Templates derived from space-filling designs (Section 4.2) originate from $m-1$ point LHSs through the hyperrectangle enclosing $\mathbf{X}_n(\check{\mathbf{x}})$, and then augmented with $\check{\mathbf{x}}$ as the mth inducing point.

Regardless of inducing point/template construction, machinery behind LIGP-based prediction is identical. Algorithm 1 outlines the steps to construct local neighborhoods and predict at each of a set of N' prediction locations $\mathbf{X}^\star$ given training data $\{\mathbf{X}_N, \mathbf{Y}_N\}$, neighborhood size n, and number of inducing points m. Each location $\mathbf{x}_i$, for $i = 1, \dots, N'$ could proceed in parallel. In our implementation we use 16 threads.[6] The pseudocode attempts to be agnostic about the inducing point scheme by simply writing IP(...). Any of Algorithms 2–4 can be used here. To estimate scale and lengthscale we used Eqs. (6–7) through simple substitutions of (m, n) for the local neighborhoods of $\mathbf{x}^\star$. We rely on `optim` in R to minimize the negative log-likelihood to estimate local $\hat{\theta}(\mathbf{x}^\star)$'s. Finally, the predictive mean and variance for $\mathbf{x}^\star$ are extracted via Eq. (8).

5.2   Borehole

Previewed in Section 4.2, the borehole function (Worley 1987) is a classic example in computer experiments literature. Outputs may be derived in closed form as

$$y = \frac{2\pi T_u [H_u - H_l]}{\log\left(\frac{r}{r_w}\right)\left[1 + \frac{2LT_u}{\log(r/r_w)r_w^2 K_w} + \frac{T_u}{T_l}\right]}$$

via inputs in the eight-dimensional rectangle:

$r_w \in [0.05, 0.15]$ $\quad$ $r \in [100, 5000]$ $\quad$ $T_u \in [63070, 115600]$ $\quad$ $T_l \in [63.1, 116]$
$H_u \in [990, 1100]$ $\quad$ $H_l \in [700, 820]$ $\quad$ $L \in [1120, 1680]$ $\quad$ $K_w \in [9855, 12045]$.

For training we use LHSs of size $N = 100000$, recoding natural inputs to the unit 8-cube followed by pre-scaling via a global separable $\hat{\theta}$ as explained in Section 5.1. We use $(m, n) = (80, 150)$ for all LIGP fits (see Appendix B). For a fair comparison, we entertain $n = 150$ for LAGP (NN) as well as the default of $n = 50$ for NN and ALC-based LAGP comparators. Figure 6 summarizes RMSEs obtained over thirty MC instances with novel training and $N' = 10000$ sized LHS testing sets.

Mirroring other studies (e.g., Sun et al. 2019), local approximation is key to using a vast training data set to get good predictions. LAGP performs better with a neighborhood of $n = 50$ selected using ALC versus even larger neighborhoods ($n = 150$) using NN. Given the smoothness of the borehole surface, the addition of "satellite" points provided by ALC gives an accuracy boost over pure NN of similar size. We believe the same to be true of LIGP (cHR). Any inducing points lying outside the neighborhood act as "satellites" in this context. This is backed up by comparable RMSE results. The added flexibility of inducing points (LIGP) over discrete subsets (LAGP) may be limited by the highly smooth borehole dynamics.

Timings are provided at the bottom of Figure 6, with LIGP LHS templates being fastest among the most competitive alternatives, accuracy-wise. Interestingly, the cHR template is even better at prediction than the optimized wIMSE one, obtained at great computational expense (3.06 minutes). Compared to LAGP (NN) with $n = 150$, accuracy is only slightly

---
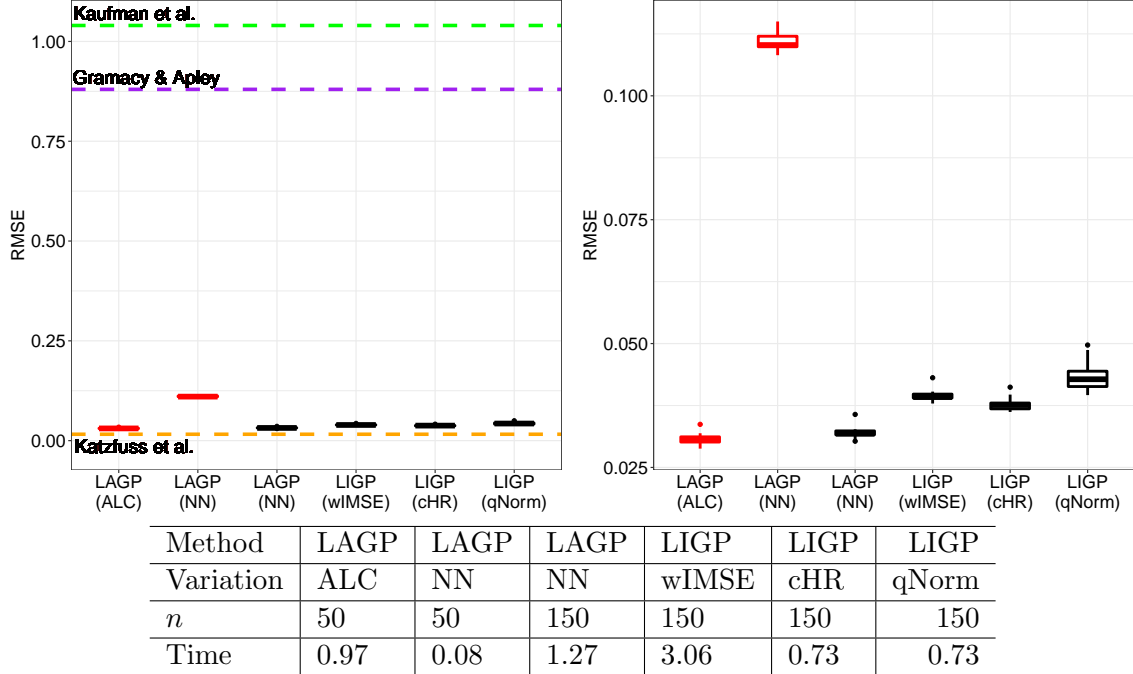
[6]I.e., two per hyperthreaded core.

Figure 6: *Top-left:* accuracy over 30 MC repetitions with lines showing other published works' results: (Kaufman et al. 2011, green), (Gramacy and Apley 2015, purple), (Katzfuss et al. 2020, orange). *Top-right:* zoomed in version focusing on the best LI/LAGP methods. The color of the boxplot outline, red and black, correspond to the sizes of the neighborhoods ($n = 50, 150$ respectively). *Table below:* compute time in minutes.

diminished, but predictions are furnished in half the time on aggregate. Again, we remind the reader that this is a little unfair to LIGP, comparing an R-only implementation to laGP's C library. Another reason this timing comparison is not more impressive is that optimizing the inducing point likelihood to obtain local $\hat{\theta}(\mathbf{x}^\star)$, despite being cubic in m rather than n, tends to take more BFGS iterations than the LAGP analog.

Although LIGP methods do not best LAGP (except NN with $n = 50$) on accuracy, it is important to place these RMSEs in context. Horizontal dashed lines in the left panel of Figure 6 offer wider historical perspective. Kaufman et al. (2011)'s reported an RMSE of 1.4 (green line; 99% sparse) with $(N, N') = (4000, 500)$ in 17 minutes via compactly supported kernels. Gramacy and Apley (2015)'s initial LAGP (ALC) implementation improved that to 0.88 (purple line) in 3 minutes, utilizing eight cores. Subsequent improvements in handling larger (less well-conditioned) matrices, and wider OpenMP parallelization bring us to the orders of magnitude more accurate and fast results in Figure 6.

More recently a method called SVecchia (Katzfuss et al. 2020), adapted from geostatistcs to computer surrogate modeling, has yielded impressive RMSEs of 0.016 (orange line) in similar exercises $((N, N') = (100000, 20000))$ in about five minutes – combining training (4.4 minutes) and testing (0.4 minutes) phases – in a single-core setting. We see this new vanguard of methods as equivalent on the borehole problem, with nuance depending on the application. For example, if you need a one-off prediction, LAGP methods (e.g., ALC) are best, furnishing accurate predictions in fractions of a second without an explicit training

phase. With modest testing sizes, LIGP methods are faster when amortizing the cost of template calculation. For larger testing sets, SVecchia methods seem attractive.

Lastly, consider comparing to a more traditional global form of inducing point prediction (Section 2.3). Using an LHS for $\bar{\mathbf{X}}_M$ with $M = 80$ in $[0, 1]^8$ requires only 0.56 minutes to produce predictions (8) with fixed lengthscale θ, less than even the space-filling template variations of LIGP. Accuracy is tightly coupled to θ, but MLEs render the method uncompetitive as a single evaluation of the log-likelihood (7) takes nine minutes.

5.3   Robot arm

The SARCOS data is a popular computer simulation benchmark from the machine learning literature (Vijayakumar and Schaal 2000; Rasmussen and Williams 2006). The data/simulations[7] model seven torque outputs as a function of 21 input variables consisting of position, velocity, and acceleration of a robot arm. It comes pre-partitioned into a training set of size $N = 44484$ and a testing set of size $N' = 4449$. Here we consider only the first torque output. High input dimensionality and non-uniform design – inputs lie on a low-dimensional manifold in the input space – present surrogates with unique challenges.

One implication of the non-uniform design for LIGP is that a hyperrectangle surrounding $\mathbf{X}_n(\check{\mathbf{x}})$, for median input $\check{\mathbf{x}}$, does not place $\check{\mathbf{x}}$ in its center. Consequently a cHR template would yield an un-centered $\mathbf{X}_m(\mathbf{x}^\star)$. Space-fillingness is preserved, albeit with many points outside of the hypersphere enclosing $\mathbf{X}_n(\check{\mathbf{x}})$. A qNorm template, by contrast, can preserve centering through Φ^{-1}. However, in both cases the low-dimensional input manifold may result in a fair number of inducing points without many $\mathbf{X}_n(\mathbf{x}^\star)$ nearby.

As with previous examples, we perform an input pre-scaling based on separable lengthscales estimated via MLE from a size $n = 1000$ random data subset. After pre-scaling we find that local likelihoods, for both LAGP and LIGP, are flat for many $\mathbf{x}^\star$, yielding exceedingly long local lengthscales $\hat{\theta}(\mathbf{x}^\star)$ and "washed out" local surrogates. Apparently, in 21 input dimensions, small neighborhoods ($n = 50$ and $n = 200$) provide insufficient information about local lengthscales, i.e., beyond the global one. Although we show results with LAGP in both variations, with and without local MLE calculations (with both isotropic and separable local kernels), all variations entertained perform much better with a fixed $\theta_0 = 1$ for all local calculations.

Figure 7 summarizes those results, plotting log RMSE against log computation time. Working from the top of the figure (lowest predictive accuracy) downwards, observe that default LAGP (blue), i.e., with local MLE lenthscales, performs worst. Larger local neighborhoods ($n = 200$ vs. $n = 50$) do not help accuracy much, and hurt speed. Separable lengthscales improve accuracy by an order of magnitude, but you do even better by sticking with a fixed $\theta_0 = 1$ after pre-scaling, which brings us to the second (red) group. Foregoing local MLE calculation conveys a several orders-of-magnitude speed-up. These RMSEs are on par with the best methods in recent studies. For example, Jankowiak and Gardner (2019) report on a bakeoff of ten deep and shallow GP and neural network comparators, with best RMSE of 0.107, which in log space is -2.3 (dashed horizontal line).[8] Keeping it simple in high dimension, especially when the training data lie on a lower-dimensional manifold, helps control estimation risk and enhances stability. Larger neighborhoods give a small accuracy fillip, but substantial increase in computation time.

---

[7]Original MATLAB: `http://www.gaussianprocess.org/gpml/data/`; plain text in our Git repo.

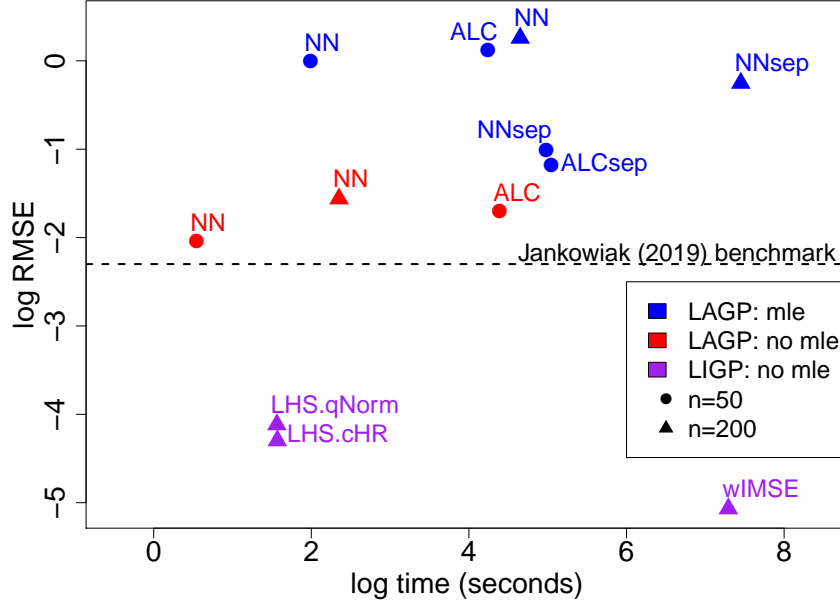[8]No timings provided; the worst method had RMSE 0.25.

Figure 7: LAGP v. LIGP models pitting log RMSE (y-axis) against log time (x-axis) on SARCOS data. LAGP fits included both isotropic and anisotropic (sep) local lengthscales. Fixing local $\theta_0 = 1$ (no mle) yields computational and predictive advantages.

Finally, LIGP methods $(m, n) = (80, 200)$ fall into the last/lowest (purple) group with the highest accuracy. These are 4-5 orders of magnitude more accurate than the default LAGP setup, 2-3 orders better than nomle-LAGP. Compute times are commensurate with the red/middle group, excepting two cases. An wIMSE template pays accuracy dividends for increased computational cost. Simple LAGP (NN) is faster but substantially less accurate. We again remind that these timings are unfair to LIGP's R-only implementation.

5.4 Satellite Drag

Finally, consider large data sets of simulated drag coefficients for satellites in low-Earth orbit. For a description of these data see Sun et al. (2019), Mehta et al. (2014), Gramacy (2020, Chapter 2.3.3) and the Git repo https://bitbucket.org/gramacylab/tpm/src. We seek accurate surrogates for drag for the Hubble Space Telescope (HST). Simulations, via so-called called test particle MC (TPMC), treat atmospheric elements of atomic oxygen (O), molecular oxygen (O_2), atomic nitrogen (N), molecular nitrogen (N_2), helium (He), or hydrogen (H) separately. Following previous studies, we consider surrogates for these "species" separately. Data for each species is comprised of a two million-sized (N) LHS over eight configuration inputs. The goal is to predict drag to a 1% relative RMSE (RMSPE) accuracy. Big training data are essential to meeting that benchmark, and needless to say ordinary large-N GP surrogates are not a viable alternative.

Figure 8 summarizes the results of 10-fold cross-validation for each species. The 1% benchmark is shown horizontally at zero in log space. Again mimicking previous experiments, we pre-scale (Section 5.1) after coding inputs and before fitting local approximations. Observe in the left panel that LAGP (NN) with $n = 150$ is the only method able to produce log RMSPEs below the 1% benchmark for all folds. However, LIGP (wIMSE) and LIGP
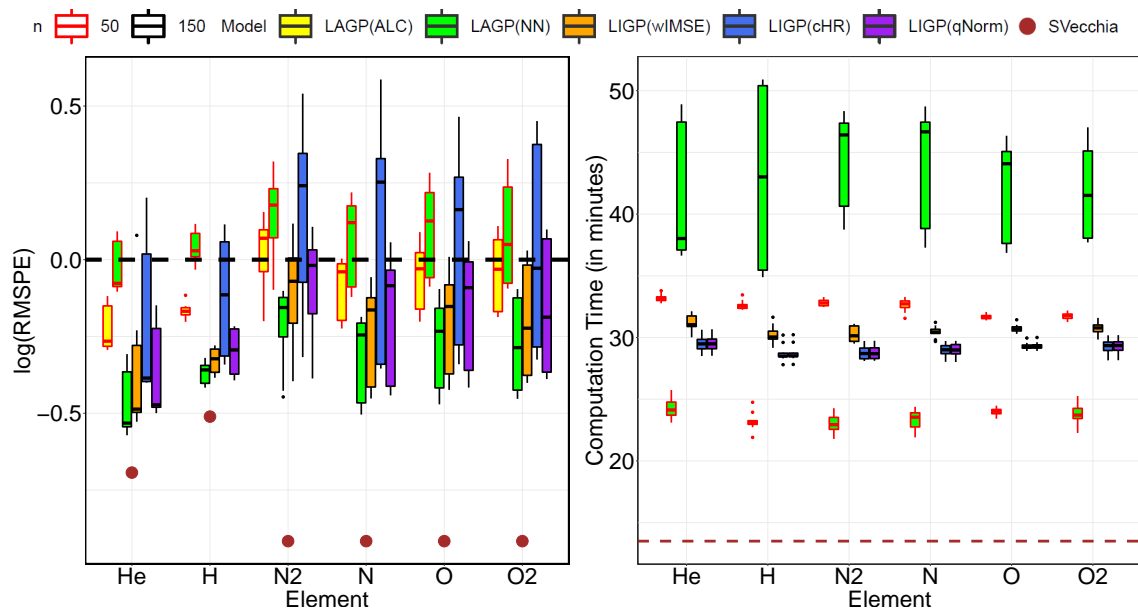
Figure 8: *Left:* accuracy over 10-fold cross validation for each species via log RMSPE. The horizontal line denotes the 1% benchmark in log space. *Right:* Prediction compute time (in minutes) across cross-validation folds.

(qNorm) come in at a close second and third and have medians (over all folds) below the 1% benchmark. Factoring in computation time (right panel), LIGP methods predict roughly 50% faster than LAGP (NN) with $n = 150$. Given the scale of the test and training sets, even LIGP (wIMSE) emerges as a viable, cheap alternative.

In contrast to the previous two examples, LIGP (cHR) accuracy suffers relative to the other space-filling template scheme LIGP (qNorm). This may be due to nonstationarity. Inducing points that lie within the neighborhood – thus motivating LIGP (qNorm) – transfer more of the flexible structure of the GP and provide more accurate predictions. Finally, results recently released using SVecchia (brown) offer further improvement, although only when substantial training time is amortized over a large predictive set. In cases when a single or a relatively small number of predictions are needed, LIGP/LAGP can furnish accurate predictions in seconds, whereas SVecchia requires (tens of) minutes.

6 Discussion

Exponential growth of diversity and size of computer simulation campaigns places a heavy burden on GP surrogates. Remaining fast enough to be useful – they cannot be slower than the simulator they are replacing – but without cutting too many corners in approximation, in order to keep fidelity high to capture nonstationary relationships, requires a nimble approach. Many interesting new methods have come online of late, including inducing points and local approximation. Inducing points address computation time and space head on, but sacrifice on fidelity. Existing likelihood based tools for choosing their multiplicity and location are difficult to wield due to an abundance of local minima. Local approximations (LAGP) perform better in prediction exercises because their criteria more squarely tar-

get predictive accuracy. However, they rely on cumbersome discrete search to supplant intractably large conditioning sets.

Here we proposed a hybrid approach: locally induced Gaussian processes (LIGPs). Toward that end, we developed a novel weighted integrated mean-squared error (wIMSE) criterion for selecting inducing points nearby predictive locations of interest. Closed forms for the criteria and derivatives were provided. The key insight here is one of replacing discrete data subset selection (LAGP) with continuous, library-based search via wIMSE through inducing points. Our empirical work revealed that such conditioning sets had a highly consistent structure from one predictive location to the next, suggesting that one-off calculations could be reused as a template for other locations of interest.

The result is a new transductive GP learner that is faster than the original, with comparable or improved accuracy in out-of-sample exercises. When LIGP results are less accurate than LAGP, the gaps are narrow and LAGP requires substantially more computation. In some cases, LIGP is orders of magnitude more accurate without demanding more computation. Our examples spanned illustrative (2d and 8d with tens and hundreds thousands of points) to high-dimensional benchmarks (21d with non-space-filling design) and real-world simulation (8d and millions of runs).

We see these promising results as providing a solid foundation from which to explore improvements: from accurate and even faster predictions; to broader application such as in low-signal and even heteroskedastic (Binois et al. 2019) stochastic simulation experiments. We have some specific ideas. Rather than NN neighborhoods for each predictive location, thrifty ALC alternatives (e.g., `alcray` in `laGP`, Gramacy and Haaland 2016) may enhance the hybrid. Kernel support could be expanded to include other families, such as Matérn, or to include locally separable lengthscales. In addition, automating the choice of local sizes (m, n) through a Bayesian optimization of out-of-sample RMSE could help make the methodology more plug-n-play.

References

Anagnostopoulos, C. and Gramacy, R. B. (2013). "Information-theoretic data discarding for dynamic trees on data streams." *Entropy*, 15, 12, 5510–5535.

Ankenman, B., Nelson, B. L., and Staum, J. (2010). "Stochastic kriging for simulation metamodeling." *Operations research*, 58, 2, 371–382.

Aune, E., Simpson, D. P., and Eidsvik, J. (2014). "Parameter estimation in high dimensional Gaussian distributions." *Statistics and Computing*, 24, 2, 247–263.

Azzimonti, D., Bect, J., Chevalier, C., and Ginsbourger, D. (2016). "Quantifying Uncertainties on Excursion Sets Under a Gaussian Random Field Prior." *SIAM/ASA Journal on Uncertainty Quantification*, 4, 1, 850–874.

Banerjee, S., Gelfand, A. E., Finley, A. O., and Sang, H. (2008). "Gaussian predictive process models for large spatial data sets." *Journal of the Royal Statistical Society. Series B: Statistical Methodology*, 70, 4, 825–848.

Barnett, S. (1979). *Matrix Methods for Engineers and Scientists*. McGraw-Hill.

Bauer, M., van der Wilk, M., and Rasmussen, C. E. (2016). "Understanding Probabilistic Sparse Gaussian Process Approximations." *Advances in Neural Information Processing Systems*, 29, 1533–1541.

Bect, J., Bachoc, F., Ginsbourger, D., et al. (2019). "A supermartingale approach to Gaussian process based sequential design of experiments." *Bernoulli*, 25, 4A, 2883–2919.

Binois, M., Huang, J., Gramacy, R. B., and Ludkovski, M. (2019). "Replication or exploration? Sequential design for stochastic simulation experiments." *Technometrics*, 61, 1, 7–23.

Burnaev, E. and Panov, M. (2015). "Adaptive design of experiments based on gaussian processes." In *International Symposium on Statistical Learning and Data Sciences*, 116–125. Springer.

Busby, D. (2009). "Hierarchical adaptive experimental design for Gaussian process emulators." *Reliability Engineering & System Safety*, 94, 7, 1183–1193.

Byrd, R. H., Lu, P., Nocedal, J., and Zhu, C. (1995). "A Limited Memory Algorithm for Bound Constrained Optimization." *SIAM Journal on Scientific Computing*, 16, 5, 1190–1208.

Carnell, R. (2019). *lhs: Latin Hypercube Samples*. R package version 1.0.1.

Chen, J., Cao, N., Low, K. H., Ouyang, R., Tan, C. K.-Y., and Jaillet, P. (2013). "Parallel Gaussian Process Regression with Low-Rank Covariance Matrix Approximations." In *Proceedings of the Twenty-Ninth Conference on Uncertainty in Artificial Intelligence*, UAI'13, 152–161. Arlington, Virginia, USA: AUAI Press.

Cohn, D. A. (1993). "Neural Network Exploration Using Optimal Experiment Design." In *Proceedings of the 6th International Conference on Neural Information Processing Systems*, NIPS'93, 679–686. San Francisco, CA, USA: Morgan Kaufmann Publishers Inc.

Csató, L. and Opper, M. (2002). "Sparse on-line Gaussian processes." *Neural computation*, 14, 3, 641–668.

Datta, A., Banerjee, S., Finley, A. O., and Gelfand, A. E. (2016). "Hierarchical Nearest-Neighbor Gaussian Process Models for Large Geostatistical Datasets." *Journal of the American Statistical Association*, 111, 514, 800–812.

Emery, X. (2009). "The kriging update equations and their application to the selection of neighboring data." *Computational Geosciences*, 13, 3, 269–280.

Fernández, F. L., Martino, L., Elvira, V., Delgado, D., and López-Santiago, J. (2020). "Adaptive Quadrature Schemes for Bayesian Inference via Active Learning." *IEEE Access*, 8, 208462–208483.

Gardner, J., Pleiss, G., Weinberger, K. Q., Bindel, D., and Wilson, A. G. (2018a). "Gpytorch: Blackbox matrix-matrix gaussian process inference with gpu acceleration." In *Advances in Neural Information Processing Systems*, 7576–7586.

Gardner, J., Pleiss, G., Wu, R., Weinberger, K., and Wilson, A. (2018b). "Product Kernel Interpolation for Scalable Gaussian Processes." In *Proceedings of the Twenty-First International Conference on Artificial Intelligence and Statistics*, eds. A. Storkey and F. Perez-Cruz, vol. 84 of *Proceedings of Machine Learning Research*, 1407–1416. PMLR.

Garton, N., Niemi, J., and Carriquiry, A. (2020). "Knot selection in sparse Gaussian processes with a variational objective function." *Statistical Analysis and Data Mining: The ASA Data Science Journal*, 324–336.

Gauthier, B. and Pronzato, L. (2014). "Spectral approximation of the IMSE criterion for optimal designs in kernel-based interpolation models." *SIAM/ASA Journal on Uncertainty Quantification*, 2, 1, 805–825.

Gorodetsky, A. and Marzouk, Y. (2016). "Mercer kernels and integrated variance experimental design: connections between Gaussian process regression and polynomial approximation." *SIAM/ASA Journal on Uncertainty Quantification*, 4, 1, 796–828.

Gramacy, R. and Haaland, B. (2016). "Speeding up neighborhood search in local Gaussian process prediction." *Technometrics*, 58, 3, 294–303.

Gramacy, R., Niemi, J., and Weiss, R. (2014). "Massively parallel approximate Gaussian process regression." *SIAM/ASA Journal on Uncertainty Quantification*, 2, 1, 564–584.

Gramacy, R. B. (2016). "`laGP`: Large-Scale Spatial Modeling via Local Approximate Gaussian Processes in `R`." *Journal of Statistical Software*, 72, 1, 1–46.

— (2020). *Surrogates: Gaussian Process Modeling, Design and Optimization for the Applied Sciences*. Boca Raton, Florida: Chapman Hall/CRC. `http://bobby.gramacy.com/surrogates/`.

Gramacy, R. B. and Apley, D. W. (2015). "Local Gaussian Process Approximation for Large Computer Experiments." *Journal of Computational and Graphical Statistics*, 24, 2, 561–578.

Gramacy, R. B. and Lee, H. K. (2008). "Bayesian treed Gaussian process models with an application to computer modeling." *Journal of the American Statistical Association*, 103, 483, 1119–1130.

— (2009). "Adaptive design and analysis of supercomputer experiments." *Technometrics*, 51, 2, 130–145.

Harville, D. A. (2011). *Matrix Algebra From a Statistician's Perspective*. Springer New York.

Hensman, J., Fusi, N., and Lawrence, N. D. (2013). "Gaussian Processes for Big Data." UAI'13, 282–290. Arlington, Virginia, USA: AUAI Press.

Hoang, T. N., Hoang, Q. M., and Low, B. K. H. (2015). "A Unifying Framework of Anytime Sparse Gaussian Process Regression Models with Stochastic Variational Inference for Big Data." In *ICML*, 569–578.

Hoffman, M. D., Blei, D. M., Wang, C., and Paisley, J. (2013). "Stochastic variational inference." *The Journal of Machine Learning Research*, 14, 1, 1303–1347.

Jankowiak, M. and Gardner, J. (2019). "Neural Likelihoods for Multi-Output Gaussian Processes." *arXiv preprint arXiv:1905.13697*.

Johnson, M. E., Moore, L., and Ylvisaker, D. (1990). "Minimax and Maximin Distance Designs." *Journal of Statistical Planning and Inference*, 26, 131–148.

Kanagawa, M. and Hennig, P. (2019). "Convergence guarantees for adaptive Bayesian quadrature methods." In *Advances in Neural Information Processing Systems*, 6237–6248.

Katzfuss, M. and Guinness, J. (2021). "A General Framework for Vecchia Approximations of Gaussian Processes." *Statist. Sci.*, 36, 1, 124–141.

Katzfuss, M., Guinness, J., and Lawrence, E. (2020). "Scaled Vecchia approximation for fast computer-model emulation." *arXiv preprint arXiv:2005.00386*.

Kaufman, C., Bingham, D., Habib, S., Heitmann, K., and Frieman, J. (2011). "Efficient emulators of computer experiments using compactly supported correlation functions, with an application to cosmology." *The Annals of Applied Statistics*, 5, 4, 2470–2492.

Kim, H. M., Mallick, B. K., and Holmes, C. C. (2005). "Analyzing nonstationary spatial data using piecewise Gaussian processes." *Journal of the American Statistical Association*, 100, 470, 653–668.

Leatherman, E. R., Santner, T. J., and Dean, A. M. (2018). "Computer experiment designs for accurate prediction." *Statistics and Computing*, 28, 4, 739–751.

Lee, H., Gramacy, R., Linkletter, C., and Gray, G. (2011). "Optimization subject to hidden constraints via statistical emulation." *Pacific Journal of Optimization*, 7, 3, 467–478.

Liu, H., Cai, J., Ong, Y.-S., and Wang, Y. (2019). "Understanding and comparing scalable Gaussian process regression for big data." *Knowledge-Based Systems*, 164, 324–335.

Mckay, D., Beckman, R., and Conover, W. (1979). "A Comparison of Three Methods for Selecting Vales of Input Variables in the Analysis of Output From a Computer Code." *Technometrics*, 21, 239–245.

Mehta, P., Walker, A., Lawrence, E., Linares, R., Higdon, D., and Koller, J. (2014). "Modeling satellite drag coefficients with response surfaces." *Advances in Space Research*, 54, 8, 1590–1607.

Morris, M. D. and Mitchell, T. J. (1995). "Exploratory Designs for Computational Experiments." *Journal of Statistical Planning and Inference*, 43, 381–402.

Neal, R. M. (1998). "Regression and Classification Using Gaussian Process Priors." *Bayesian Statistics*, 6, 475–501.

Pleiss, G., Gardner, J., Weinberger, K., and Wilson, A. G. (2018). "Constant-Time Predictive Distributions for Gaussian Processes." In *Proceedings of the 35th International Conference on Machine Learning*, eds. J. Dy and A. Krause, vol. 80, 4114–4123. Stockholmsmässan, Stockholm Sweden: PMLR.

Poggio, T. and Girosi, F. (1990). "Networks for approximation and learning." *Proceedings of the IEEE*, 78, 1481 – 1497. Eq. 25.

Pratola, M. T., Harari, O., Bingham, D., and Flowers, G. E. (2017). "Design and analysis of experiments on nonconvex regions." *Technometrics*, 59, 1, 36–47.

Quiñonero, J. and Rasmussen, C. (2005). "A Unifying View of Sparse Approximate Gaussian Process Regression." *Journal of Machine Learning Research*, 6, 1939–1959.

R Core Team (2020). *R: A Language and Environment for Statistical Computing*. R Foundation for Statistical Computing, Vienna, Austria.

Rasmussen, C. E. and Williams, C. K. I. (2006). *Gaussian Processes for Machine Learning*. Adaptive Computation and Machine Learning. Cambridge, MA, USA: MIT Press.

Sacks, J., Welch, W. J., Mitchell, T. J., and Wynn, H. P. (1989). "Design and analysis of computer experiments." *Statistical science*, 409–423.

Santner, T., Williams, B., and Notz, W. (2018). *The Design and Analysis Computer Experiments*. Springer; 2nd edition.

Schürch, M., Azzimonti, D., Benavoli, A., and Zaffalon, M. (2020). "Recursive estimation for sparse Gaussian process regression." *Automatica*, 120, 109127.

Seeger, M., Williams, C., and Lawrence, N. (2003). "Fast forward selection to speed up sparse Gaussian process regression." *Proceedings - 9th International Conference on Artificial Intelligence and Statistics (AISTATS 2003)*, 9.

Seo, S., Wallat, M., Graepel, T., and Obermayer, K. (2000). "Gaussian process regression: Active data selection and test point rejection." In *Mustererkennung 2000*, 27–34. Springer.

Smola, A. J. and Bartlett, P. L. (2001). "Sparse Greedy Gaussian Process Regression." In *Advances in Neural Information Processing Systems 13*, eds. T. K. Leen, T. G. Dietterich, and V. Tresp, 619–625. MIT Press.

Snelson, E. and Ghahramani, Z. (2006). "Sparse Gaussian Processes using Pseudo-inputs." *Advances in Neural Information Processing Systems 18*, 1257–1264.

Solin, A. and Särkkä, S. (2020). "Hilbert space methods for reduced-rank Gaussian process regression." *Statistics and Computing*, 30, 2, 419–446.

Stein, M., Chi, Z., and Welty, L. (2004). "Approximating likelihoods for large spatial data sets." *Journal of the Royal Statistical Society: Series B (Statistical Methodology)*, 66, 2, 275–296.

Stein, M. L. (2012). *Interpolation of Spatial Data: Some Theory for Kriging*. Springer Series in Statistics. Springer New York.

Sun, F., Gramacy, R., Haaland, B., Lawrence, E., and Walker, A. (2019). "Emulating satellite drag from large simulation experiments." *IAM/ASA Journal on Uncertainty Quantification*, 7, 2, 720–759.

Sung, C., Gramacy, R., and Haaland, B. (2018). "Exploiting variance reduction potential in local Gaussian process search." *Statistica Sinica*, 28, 577–600.

Svendsen, D. H., Martino, L., and Camps-Valls, G. (2020). "Active emulation of computer codes with Gaussian processes–Application to remote sensing." *Pattern Recognition*, 100, 107103.

Tan, L. S., Ong, V. M., Nott, D. J., and Jasra, A. (2016). "Variational inference for sparse spectrum Gaussian process regression." *Statistics and Computing*, 26, 6, 1243–1261.

Titsias, M. (2009a). "Variational learning of inducing variables in sparse Gaussian processes." In *Artificial Intelligence and Statistics*, 567–574.

— (2009b). "Variational Learning of Inducing Variables in Sparse Gaussian Processes." In *Proceedings of the Twelth International Conference on Artificial Intelligence and Statistics*, eds. D. van Dyk and M. Welling, vol. 5 of *Proceedings of Machine Learning Research*, 567–574. PMLR.

Ubaru, S., Chen, J., and Saad, Y. (2017). "Fast Estimation of tr(f(A)) via Stochastic Lanczos Quadrature." *SIAM Journal on Matrix Analysis and Applications*, 38, 4, 1075–1099.

Vapnik, V. (2013). *The Nature of Statistical Learning Theory*. New York, NY: Springer Science & Business Media.

Vecchia, A. (1988). "Estimation and model identification for continuous spatial processes." *Journal of the Royal Statistical Society: Series B (Methodological)*, 50, 2, 297–312.

Vijayakumar, S. and Schaal, S. (2000). "Locally weighted projection regression: An o (n) algorithm for incremental real time learning in high dimensional space." In *Proceedings of the Seventeenth International Conference on Machine Learning (ICML 2000)*, vol. 1, 288–293.

Wahba, G. (1990). *Spline Models for Observational Data*. Philadelphia: Society for Industrial and Applied Mathematics. Ch. 7.

Wang, H. and Li, J. (2018). "Adaptive Gaussian process approximation for Bayesian inference with expensive likelihood functions." *Neural computation*, 30, 11, 3072–3094.

Wang, K., Pleiss, G., Gardner, J., Tyree, S., Weinberger, K. Q., and Wilson, A. G. (2019). "Exact Gaussian processes on a million data points." In *Advances in Neural Information Processing Systems*, 14622–14632.

Williams, C. K. I. and Seeger, M. (2001). "Using the Nyström Method to Speed Up Kernel Machines." In *Advances in Neural Information Processing Systems 13*, eds. T. K. Leen, T. G. Dietterich, and V. Tresp, 682–688. MIT Press.

Wilson, A. and Nickisch, H. (2015). "Kernel interpolation for scalable structured Gaussian processes (KISS-GP)." In *International Conference on Machine Learning*, 1775–1784.

Worley, B. A. (1987). "Deterministic uncertainty analysis." Tech. rep., Oak Ridge National Lab., TN (USA).

Zhang, B., Cole, D. A., and Gramacy, R. B. (2021). "Distance-Distributed Design for Gaussian Process Surrogates." *Technometrics*, 63, 1, 40–52.

A   IMSE and ALC overview

As mentioned in Section 2.3, variance-based sequential design criteria are better aligned with the goal of generating accurate GP predictions than using the likelihood. We consider variations on integrated mean-squared error (IMSE) over a domain $\mathcal{X}$, with smaller being better:

$$(\text{IMSE}) \qquad I = \int_{\tilde{\mathbf{x}} \in \mathcal{X}} \sigma^2(\tilde{\mathbf{x}}) \, d\tilde{\mathbf{x}}.$$

Choose $\sigma^2(\cdot) \equiv \sigma_N^2(\cdot)/\nu$ from Eq. (2), and I may be used to optimize the N coordinates of $\mathbf{X}_N$, or to choose the next $(N+1^{\text{st}})$ one $(\tilde{\mathbf{x}}_{N+1})$ in a sequential setting.[9] Closed form expressions are available for rectangular $\mathcal{X}$ and common kernels (e.g., Ankenman et al. 2010; Anagnostopoulos and Gramacy 2013; Burnaev and Panov 2015; Leatherman et al. 2018). Analytic derivatives $\frac{\partial I}{\partial \tilde{\mathbf{x}}_{N+1}}$ facilitate numerical optimization (Binois et al. 2019; Gramacy 2020, Chapters 4 & 10). Approximations are common otherwise (Gramacy and Lee 2009; Gauthier and Pronzato 2014; Gorodetsky and Marzouk 2016; Pratola et al. 2017).

An analogue active learning heuristic from Cohn (1993), dubbed ALC, instead targets variance aggregated over a discrete reference set $\mathcal{X}$, originally for neural network surrogates:

$$(\text{ALC}) \qquad \Delta\sigma^2 = \sum_{\tilde{\mathbf{x}} \in \mathcal{X}} \sigma^2(\tilde{\mathbf{x}}) - \sigma_{\text{new}}^2(\tilde{\mathbf{x}}),$$

Seo et al. (2000) ported ALC to GPs taking $\sigma^2(\cdot) = \sigma_N^2(\cdot)$ and $\sigma_{\text{new}}^2(\cdot) \equiv \sigma_{N+1}^2(\cdot)$. If discrete and volume-based $\mathcal{X}$ are similar, then $\Delta\sigma^2 \approx c - I$, where c is constant on $\mathbf{x}_{N+1}$. Discrete $\Delta\sigma^2$ via ALC is advantageous in transductive learning settings (Vapnik 2013), where $\mathcal{X}$ can be matched with a testing set. Otherwise, analytic I via IMSE may be preferred.

Against that backdrop, we propose employing ALC and IMSE to select inducing points $\bar{\mathbf{X}}_M$. To our knowledge, using such variance-based criteria is novel in the literature on the selection of inducing points. The criteria below are framed sequentially, for an $M + 1^{\text{st}}$ point given M collected already. Although we prefer this greedy approach – optimizing d coordinates one-at-a-time rather than Md all at once in a surface with many equivalent locally optimal configurations due to label-switching – either criteria is easily re-purposed

---

[9]Dividing out ν removes dependence on $\mathbf{Y}$-values through $\hat{\nu}$. Greedy build-up of $\mathbf{x}_{n+1}$ over $n = N_0, \ldots, N-1$ is near optimal due to a supermartingale property (Bect et al. 2019).

for an all-at-once application. Under the diagonal-corrected Nyström approximation (3) and assuming coded $\mathcal{X} = [0,1]^d$,

$$\text{ALC}_N^{(M+1)} = \text{ALC}(\bar{\mathbf{x}}_{M+1}; \mathbf{X}_N, \mathbf{Y}_N, \mathcal{X}, \bar{\mathbf{X}}_M) = c - \sum_{\tilde{\mathbf{x}} \in \mathcal{X}} \sigma^2_{M+1,N}(\tilde{\mathbf{x}}), \quad \text{and} \tag{13}$$

$$\text{IMSE}_N^{(M+1)} = \text{IMSE}(\bar{\mathbf{x}}_{M+1}, \mathbf{X}_N, \mathbf{Y}_N, \mathcal{X}, \bar{\mathbf{X}}_M) = E - \text{tr}\left\{ \left(\mathbf{K}_{M+1}^{-1} - \mathbf{Q}_{M+1}^{-1(N)} \right) \mathbf{W}_{M+1} \right\},$$

where $E = \int_{\tilde{x} \in \mathcal{X}} k(\tilde{\mathbf{x}}, \tilde{\mathbf{x}}) d\tilde{\mathbf{x}}$ and $\mathbf{W}_{M+1}$ is $(M+1) \times (M+1)$ via $w(\bar{\mathbf{x}}_i, \bar{\mathbf{x}}_j) = \int_{\tilde{\mathbf{x}} \in \mathcal{X}} k(\bar{\mathbf{x}}_i, \tilde{\mathbf{x}}) k(\bar{\mathbf{x}}_j, \tilde{\mathbf{x}}) d\tilde{\mathbf{x}}$ for $i, j \in \{1, ..., M+1\}$. This derivation is similar to the wIMSE calculations (10) and (11) following Binois et al. (2019).
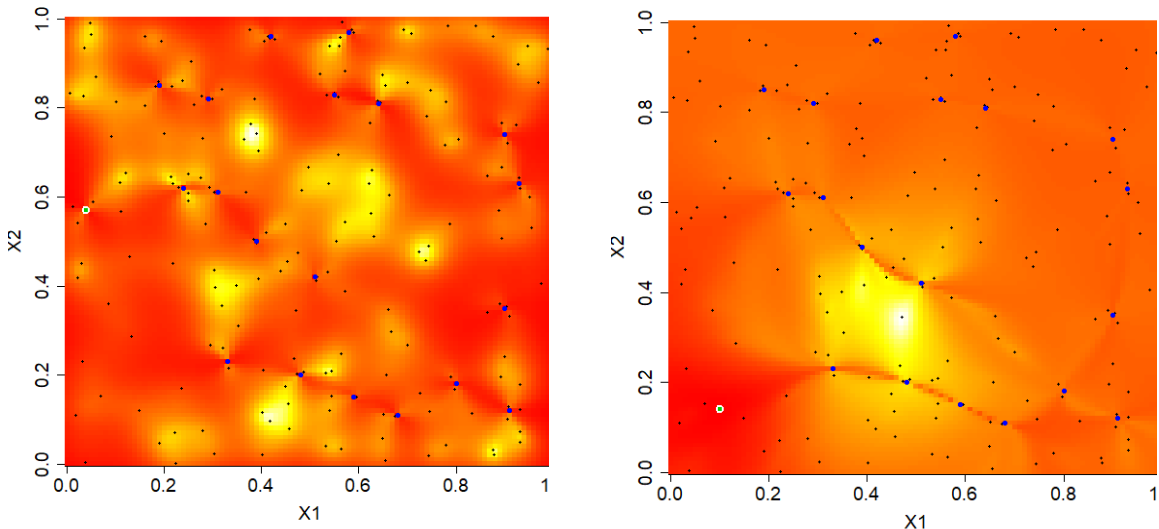
(a) Variational lower bound of log-likelihood surface

(b) ALC/IMSE surface

Figure 9: In both panels: $N = 200$ training data points (black dots) and $M = 19$ inducing points (blue dots), selecting the twentieth one (green) by two criteria: (a) variational lower bound of the log-likelihood; (b) ALC/IMSE. Yellow is higher/red lower.

To explore inducing point optimization, consider Herbie's tooth (Lee et al. 2011) described in Section 2.3. Figure 9 shows variational lower-bound of the log-likelihood (left) and ALC/IMSE surfaces (right) for $\bar{\mathbf{x}}_{20}$ given a modestly sized training dataset $(\mathbf{X}_N, \mathbf{Y}_N)$ of size $N = 200$. Similarities in the two surfaces are apparent. Many low/red areas coincide, but the optimizing locations (green dots), found via multi-start local optimization with identically fixed kernel hyperparameters, do not. Even after taking great care to humbly restrict searchers, e.g., from crossing $\bar{\mathbf{X}}_M$ locations, sometimes upwards of 1000 evaluations were required to achieve convergence. Consequently, quadratic ALC/IMSE is faster.

A.1 Derivations of wIMSE and its gradient

For the predictive location $\mathbf{x}^*$, assign weight $k_\theta(\tilde{\mathbf{x}}, \mathbf{x}^\star)$ and consider squared exponential kernel $k_\theta(\cdot, \cdot)$ with isotropic lengthscale (1). The following is based on predictive variance (8) and expectation of the quadratic form of a random vector (Binois et al. 2019, Section

3.1).

$$\text{wIMSE}(\bar{\mathbf{x}}_{m+1}, \mathcal{X}, \bar{\mathbf{X}}_m, \mathbf{X}_n, \theta, \mathbf{x}^\star) = \int_{\tilde{\mathbf{x}} \in \mathcal{X}} k_\theta(\tilde{\mathbf{x}}, \mathbf{x}^\star) \sigma^2_{n,m+1}(\tilde{\mathbf{x}}) \ d\tilde{\mathbf{x}}$$

$$= \int_{\tilde{\mathbf{x}} \in \mathcal{X}} k_\theta(\tilde{\mathbf{x}}, \mathbf{x}^\star) \Big(k_\theta(\tilde{\mathbf{x}}, \tilde{\mathbf{x}}) + \epsilon_K - k_\theta(\tilde{\mathbf{x}}, \bar{\mathbf{X}}_{m+1}) \Big[\mathbf{K}_{m+1}^{-1} - \mathbf{Q}_{m+1}^{-1(n)} \Big] k_\theta(\tilde{\mathbf{x}}, \bar{\mathbf{X}}_{m+1})^\top \Big) d\tilde{\mathbf{x}}$$

$$= \prod_{k=1}^{D} \Big((1 + \epsilon_K) \int_{a_k}^{b_k} k_\theta(\tilde{\mathbf{x}}_k, \mathbf{x}_k^\star) d\tilde{\mathbf{x}}_k$$

$$\quad - \int_{a_k}^{b_k} k_\theta(\tilde{\mathbf{x}}_k, \mathbf{x}_k^\star)^{1/2} k_\theta(\tilde{\mathbf{x}}_k, \bar{\mathbf{X}}_{m+1,k}) \Big[\mathbf{K}_{m+1}^{-1} - \mathbf{Q}_{m+1}^{-1(n)} \Big] \times k_\theta(\tilde{\mathbf{x}}_k, \bar{\mathbf{X}}_{m+1,k})^\top k_\theta(\tilde{\mathbf{x}}_k, \mathbf{x}_k^\star)^{1/2} \ d\tilde{\mathbf{x}}_k \Big)$$

$$= \frac{\sqrt{\theta\pi}(1 + \epsilon_K)^D}{2} \prod_{k=1}^{D} \Big(\text{erf} \Big\{ \frac{\mathbf{x}^\star - a_k}{\sqrt{\theta}} \Big\} - \text{erf} \Big\{ \frac{\mathbf{x}^\star - b_k}{\sqrt{\theta}} \Big\} \Big) - \text{tr} \Big\{ (\mathbf{K}_{m+1}^{-1} - \mathbf{Q}_{m+1}^{-1}) \mathbf{W}_{m+1}^\star \Big\}$$

where $\mathbf{W}_{m+1}^\star = \prod_{k=1}^{D} \mathbf{W}_{m+1,k}^\star$ in D dimensions. The entry in the ith row and j^{th} column of $\mathbf{W}_{m+1,k}^\star$ is

$$w_{m+1,k}^{\star(i,j)} \equiv w_{m+1,k}^\star(\bar{\mathbf{x}}_{i,k}, \bar{\mathbf{x}}_{j,k})$$

$$= \int_{a_k}^{b_k} k_\theta(\tilde{\mathbf{x}}_k, \mathbf{x}_k^\star) k_\theta(\tilde{\mathbf{x}}_k, \bar{\mathbf{x}}_{i,k}) k_\theta(\tilde{\mathbf{x}}_k, \bar{\mathbf{x}}_{j,k}) d\tilde{\mathbf{x}}_k$$

$$= \int_{a_k}^{b_k} \exp \Big\{ -\frac{(\tilde{\mathbf{x}}_k - \mathbf{x}_k^\star)^2 + (\tilde{\mathbf{x}}_k - \bar{\mathbf{x}}_{i,k})^2 + (\tilde{\mathbf{x}}_k - \bar{\mathbf{x}}_{j,k})^2}{\theta} \Big\} d\tilde{\mathbf{x}}_k$$

$$= \sqrt{\frac{\pi\theta}{12}} \exp \Big\{ \frac{2}{3\theta} (\bar{\mathbf{x}}_{i,k} \mathbf{x}_k^\star + \bar{\mathbf{x}}_{j,k} \mathbf{x}_k^\star + \bar{\mathbf{x}}_{i,k} \bar{\mathbf{x}}_{j,k} - \mathbf{x}_k^{\star 2} - \bar{\mathbf{x}}_{i,k}^2 - \bar{\mathbf{x}}_{j,k}^2) \Big\} \times$$

$$\Big(\text{erf} \Big\{ \frac{\iota_k^{(i,j)} - 3a_k}{\sqrt{3\theta}} \Big\} - \text{erf} \Big\{ \frac{\iota_k^{(i,j)} - 3b_k}{\sqrt{3\theta}} \Big\} \Big)$$

where $\iota_k^{(i,j)} = \mathbf{x}_k^\star + \bar{\mathbf{x}}_{i,k} + \bar{\mathbf{x}}_{j,k}$. $\bar{\mathbf{x}}_{i,k}, \bar{\mathbf{x}}_{j,k}$ are entries from the ith and j^{th} rows and k^{th} column of $\bar{\mathbf{X}}_{m+1}$ $(i, j \in \{1, \ldots, m+1\})$ and $\mathbf{x}_k^\star$ is the kth coordinate of $\mathbf{x}^\star$.

The gradient of weighted integrated mean-squared error with respect to the kth dimension of $\bar{\mathbf{x}}_{m+1}$ is:

$$\frac{\partial \text{wIMSE}(\bar{\mathbf{x}}_{m+1}, \mathcal{X}, \bar{\mathbf{X}}_m, \mathbf{X}_n, \theta, \mathbf{x}^\star)}{\partial \bar{\mathbf{x}}_{m+1,k}}$$

$$= -\text{tr} \Big\{ \Big(\frac{\partial \mathbf{K}_{m+1}^{-1}}{\partial \bar{\mathbf{x}}_{m+1,k}} - \frac{\partial \mathbf{Q}_{m+1}^{-1(n)}}{\partial \bar{\mathbf{x}}_{m+1,k}} \Big) \mathbf{W}_{m+1}^\star \Big\} - \text{tr} \Big\{ \Big(\mathbf{K}_{m+1}^{-1} - \mathbf{Q}_{m+1}^{-1(n)} \Big) \frac{\partial \mathbf{W}_{m+1}^\star}{\partial \bar{\mathbf{x}}_{m+1,k}} \Big\}$$

$$= \text{tr} \Big\{ \Big(\mathbf{K}_{m+1}^{-1} \frac{\partial \mathbf{K}_{m+1}}{\partial \bar{\mathbf{x}}_{m+1,k}} \mathbf{K}_{m+1}^{-1} - \mathbf{Q}_{m+1}^{-1(n)} \frac{\partial \mathbf{Q}_{m+1}^{(n)}}{\partial \bar{\mathbf{x}}_{m+1,k}} \mathbf{Q}_{m+1}^{-1(n)} \Big) \mathbf{W}_{m+1}^\star \Big\}$$

$$\quad - \text{tr} \Big\{ \Big(\mathbf{K}_{m+1}^{-1} - \mathbf{Q}_{m+1}^{-1(n)} \Big) \frac{\partial \mathbf{W}_{m+1}^\star}{\partial \bar{\mathbf{x}}_{m+1,k}} \Big\}$$

In the matrix $\frac{\partial \mathbf{W}^\star_{m+1}}{d\bar{\mathbf{x}}_{m+1,k}}$, all entries are zero except the row/column that corresponds to the row of $\bar{\mathbf{X}}_{m+1}$ that contains $\bar{\mathbf{x}}_{m+1}$, which we place in the last $m+1^{\text{st}}$ row. For the nonzero entries in $\frac{\partial \mathbf{W}^\star_{m+1}}{\partial \bar{\mathbf{x}}_{m+1,k}}$, we re-express them as

$$\frac{\partial w^\star_{m+1}(\bar{\mathbf{x}}_i, \bar{\mathbf{x}}_{m+1})}{\partial \bar{\mathbf{x}}_{m+1,k}} = \frac{\partial w^{\star(i,m+1)}_{m+1}}{\partial \bar{\mathbf{x}}_{m+1,k}} \prod_{k'=1, k' \neq k}^{D} w^{\star(i,m+1)}_{m+1,k'}$$

where

$$\frac{\partial w^{\star(i,m+1)}_{m+1}}{\partial \bar{\mathbf{x}}_{m+1,k}} = \sqrt{\frac{\pi\theta}{12}} \exp\left\{ \frac{2}{3\theta}\left(\bar{\mathbf{x}}_{i,k}\mathbf{x}^\star_k + \bar{\mathbf{x}}_{m+1,k}\mathbf{x}^\star_k + \bar{\mathbf{x}}_{i,k'}\bar{\mathbf{x}}_{m+1,k} - \mathbf{x}^{*2}_k - \bar{\mathbf{x}}^2_{i,k} - \bar{\mathbf{x}}^2_{m+1,k} \right) \right\}$$

$$\times \left[\frac{2}{3\theta}(\mathbf{x}^\star_k - 2\bar{\mathbf{x}}_{m+1,k} - \bar{\mathbf{x}}_{i,k}) \times \left(\mathrm{erf}\left\{ \frac{\iota^{(i,m+1)}_k - 3a_k}{\sqrt{3\theta}} \right\} - \mathrm{erf}\left\{ \frac{\iota^{(i,m+1)}_k - 3b_k}{\sqrt{3\theta}} \right\} \right) \right.$$

$$\left. + \frac{2}{\sqrt{3\pi\theta}}\left(\exp\left\{ -\frac{(\iota^{(i,m+1)}_k - 3a_k)^2}{3\theta} \right\} - \exp\left\{ -\frac{(\iota^{(i,m+1)}_k - 3b_k)^2}{3\theta} \right\} \right) \right].$$

Working with $\mathbf{K}_{m+1}$ and $\mathbf{Q}^{(n)}_{m+1}$ is cubic in m, yet even that is overkill. Thrifty evaluation of Eqs. (10–12) lies in construction of $\mathbf{Q}^{(n)}_{m+1}$ which is equivalent to $\mathbf{K}_{m+1} + \mathbf{k}^\top_{n,m+1}\boldsymbol{\Gamma}_{n,m+1}$. Evaluating $\mathbf{k}^\top_{n,m+1}\boldsymbol{\Gamma}_{n,m+1}$ requires $2n-1$ products for each of $(m+1)^2$ entries, incurring costs in $\mathcal{O}(m^2 n)$ flops. Assuming $n \gg m$, this dominates the $\mathcal{O}(m^3)$ cost of decomposition.

More time can be saved through partitioned inverse (Barnett 1979) sequential updates to $\mathbf{K}^{-1}_{m+1}$ after the new $\bar{\mathbf{x}}_{m+1}$ is chosen, porting LAGPs frugal updates to the LIGP context. Writing $\mathbf{K}_{m+1}$ as an m-submatrix with new $m+1^{\text{st}}$ column gives

$$\mathbf{K}_{m+1} = \begin{bmatrix} \mathbf{K}_m & \mathbf{k}_m(\bar{\mathbf{x}}_{m+1}) \\ \mathbf{k}_m(\bar{\mathbf{x}}_{m+1})^\top & k_\theta(\bar{\mathbf{x}}_{m+1}, \bar{\mathbf{x}}_{m+1}) \end{bmatrix} \text{ so that } \mathbf{K}^{-1}_{m+1} = \begin{bmatrix} \mathbf{K}^{-1}_m + \rho\boldsymbol{\eta}\boldsymbol{\eta}^\top & \boldsymbol{\eta} \\ \boldsymbol{\eta}^\top & \rho^{-1} \end{bmatrix} \quad (14)$$

using $\rho = k_\theta(\bar{\mathbf{x}}_{m+1}, \bar{\mathbf{x}}_{m+1}) - \mathbf{k}^\top_m(\bar{\mathbf{x}}_{m+1})\mathbf{K}^{-1}_m\mathbf{k}_m(\bar{\mathbf{x}}_{m+1})$ and m-length column vector $\boldsymbol{\eta} = -\rho^{-1}\mathbf{K}^{-1}_m\mathbf{k}_m(\bar{\mathbf{x}}_{m+1})$. Updating $\mathbf{K}^{-1}_{m+1}$ requires calculation of ρ, $\boldsymbol{\eta}$, and $\boldsymbol{\eta}\boldsymbol{\eta}^\top$, each of which is in $\mathcal{O}(m^2)$. Thus we reduce the computational complexity of $\mathbf{K}^{-1}_{m+1}$ from $\mathcal{O}(m^3)$ to $\mathcal{O}(m^2)$. Similar partitioning provides sequential updates to $\Omega^{(m+1)}_n$, a diagonal matrix:

$$\Omega^{(m+1)}_n = \mathrm{Diag}\left(\mathbf{K}_n + \epsilon_K \mathbb{I}_n - \mathbf{k}_{n,m+1}\mathbf{K}^{-1}_{m+1}\mathbf{k}^\top_{n,m+1} \right)$$

$$= \Omega^{(m)}_n - \rho^{-1}\mathrm{Diag}\left\{ \zeta\zeta^\top \right\} \quad (15)$$

where $\zeta = \mathbf{k}_{nm}\mathbf{K}^{-1}_m\mathbf{k}_m(\bar{\mathbf{x}}_{m+1}) - \mathbf{k}_n(\bar{\mathbf{x}}_{m+1})$. Updates of $\Omega^{(m+1)}_n$ without partitioning, driven by matrix–vector product(s) $\mathbf{k}_{n,m+1}\mathbf{K}^{-1}_{m+1}\mathbf{k}^\top_{n,m+1}$ involve $m^2 n$ flops. Using (15) reduces that to $\mathcal{O}(mn)$.

Unlike in Eq. (14), $\mathbf{Q}^{(n)}_m$ cannot be trivially augmented to construct $\mathbf{Q}^{(n)}_{m+1}$ due to the presence of $\Omega^{(m)}_n$ which is also embedded in $\mathbf{Q}^{(n)}_m$. Yet there are some time savings to be found in the partitioned inverse

$$\mathbf{Q}^{(n)}_{m+1} = \begin{bmatrix} \mathbf{Q}^{(n)}_{m*} & \boldsymbol{\gamma}(\bar{\mathbf{x}}_{m+1}) \\ \boldsymbol{\gamma}(\bar{\mathbf{x}}_{m+1})^\top & \psi(\bar{\mathbf{x}}_{m+1}) \end{bmatrix} \quad \mathbf{Q}^{-1(n)}_{m+1} = \begin{bmatrix} \mathbf{Q}^{-1(n)}_{m*} + \upsilon\boldsymbol{\xi}\boldsymbol{\xi}^\top & \boldsymbol{\xi} \\ \boldsymbol{\xi}^\top & \upsilon^{-1} \end{bmatrix} \quad (16)$$

with $\mathbf{Q}_{m*}^{(n)} = \mathbf{K}_m + \mathbf{k}_{nm}^\top \Omega_n^{(m+1)-1} \mathbf{k}_{nm}$ built via updated values of $\Omega_n^{(m+1)}$, $\boldsymbol{\gamma}(\bar{\mathbf{x}}_{m+1}) = \mathbf{k}_m(\bar{\mathbf{x}}_{m+1}) + \mathbf{k}_{nm}^\top \Omega_n^{-1(m+1)} \mathbf{k}_n(\bar{\mathbf{x}}_{m+1})$, $\psi(\bar{\mathbf{x}}_{m+1}) = k_\theta(\bar{\mathbf{x}}_{m+1}, \bar{\mathbf{x}}_{m+1}) + k_n(\bar{\mathbf{x}}_{m+1})^\top \Omega_n^{-1(m+1)} k_n(\bar{\mathbf{x}}_{m+1})$, $\upsilon = \psi(\bar{\mathbf{x}}_{m+1}) - \boldsymbol{\gamma}(\bar{\mathbf{x}}_{m+1})^\top \mathbf{Q}_{m*}^{-1(n)} \boldsymbol{\gamma}(\bar{\mathbf{x}}_{m+1})$ and $\xi = -\upsilon^{-1} \mathbf{Q}_{m*}^{-1(n)} \boldsymbol{\gamma}(\bar{\mathbf{x}}_{m+1})$. Similar to $\mathbf{Q}_m^{(n)}$, calculating $\mathbf{Q}_{m*}^{(n)}$ requires in flops in $\mathcal{O}(m^2 n)$. Consequently the entire scheme can be managed in $\mathcal{O}(m^2 n)$.

B Determining neighborhood size

Little attention is paid in the literature to the choosing the number of (global) inducing points (Seeger et al. 2003; Titsias 2009b; Azzimonti et al. 2016) relative to problem size (N, d), except on computational grounds – smaller M is better. The same is true for local neighborhood size n in LAGP. Although there is evidence that the `laGP` default of $n = 50$ is too small (Gramacy 2016), especially with larger input dimension d, cubically growing expense in n limits the efficacy of larger n in practice. With local inducing points this is mitigated through cubic-in-m proxies, allowing larger local neighborhoods, thus implying more latitude to explore/choose good (m, n) combinations.

Toward that end, we considered a coarse grid of (m, n) and predictive RMSEs on Herbie's tooth ($d = 2$) and borehole ($d = 8$) toy problems. Setup details are identical to descriptions in Sections 3.2 and 5.2, respectively, and we used the qNorm (Φ^{-1}) template throughout. An LHS testing set of size $N' = 1000$ was used to generate the response surfaces of RMSEs reported in Figure 10. These are shown in log space for a more visually appealing color scheme, and were obtained after GP smoothing to remove any artifacts from random testing. Grid elements where $m > n$ were omitted from the simulation on the grounds that there are no run-time benefits to those choices.
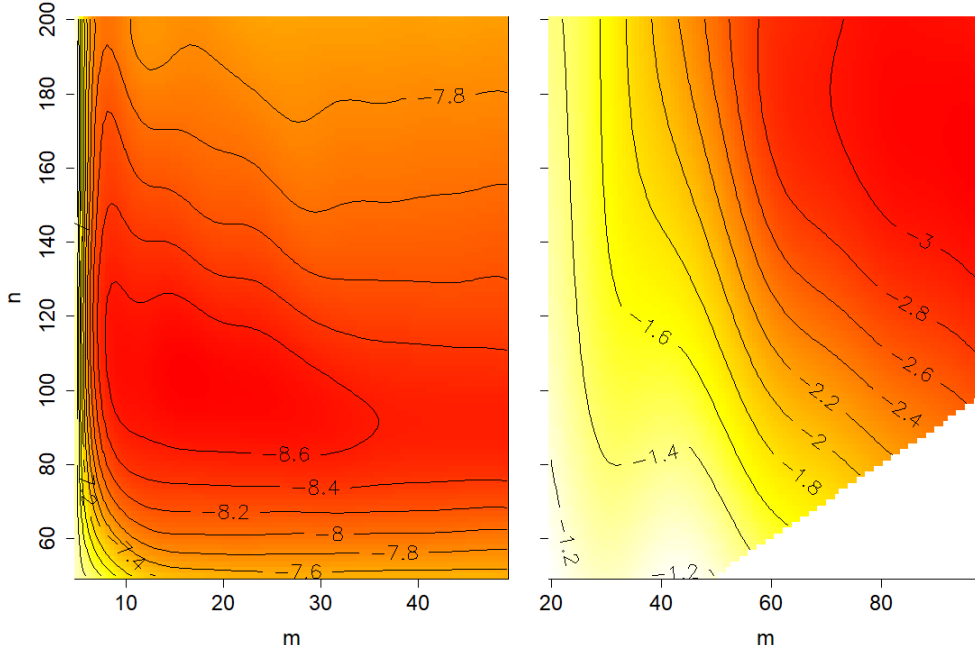

Figure 10: log(RMSE) over inducing points m and neighborhood n: Herbie's tooth (left) and borehole (right).

Observe that both surfaces are fairly flat across a wide swath of m, excepting quick ascent (decrease in accuracy) for smaller numbers of inducing points in the left panel. The situation is similar for n. Best settings are apparently input-dimension dependent. Numbers of inducing points as low as $m = 10$ seems sufficient in 2d (top panel), whereas $m = 80$ is needed in 8d. For borehole, it appears that larger neighborhoods n are better, perhaps because the response surface is very smooth and the likelihood prefers long lengthscales (Gramacy 2016). A setting like $n = 150$ seems to offer good results without being too large. The situation is different for Herbie's tooth. Here larger n has deleterious effects. Its non-stationary nature demands reactivity which is proffered by smaller local neighborhood. A setting of $n = 100$ looks good.

These are just two problems, and it is clearly not reasonable to grid-out (m, n) space for all future applications. But nevertheless we have found that these rules of thumb port well to our empirical work in Section 5. Our satdrag example ($d = 8$) and classic $d = 21$ benchmark work well with the settings found for borehole, for example. Some ideas for automating the choice of (m, n) are discussed in Section 6.